

# Development of a 3 x 3 Micromachined 190 GHz SIS Imaging Array

by

Konstantinos Konistis

Submitted to the Department of Electrical Engineering and Computer  
Science

in partial fulfillment of the requirements for the degree of

Master of Science in Electrical Engineering and Computer Science

at the

MASSACHUSETTS INSTITUTE OF TECHNOLOGY

May 1998

© Massachusetts Institute of Technology 1998. All rights reserved.

Author .....  
Department of Electrical Engineering and Computer Science  
May 11, 1998

Certified by .....  
Qing Hu  
Associate Professor of Electrical Engineering and Computer Science  
Thesis Supervisor

Accepted by .....  
Arthur C. Smith  
Chairman, Departmental Committee on Graduate Students



# Development of a 3 x 3 Micromachined 190 GHz SIS Imaging Array

by

Konstantinos Konistis

Submitted to the Department of Electrical Engineering and Computer Science  
on May 11, 1998, in partial fulfillment of the  
requirements for the degree of  
Master of Science in Electrical Engineering and Computer Science

## Abstract

This thesis studies the design, fabrication, and characterization of a 3x3 micromachined SIS imaging array. The 3x3 array consists of  $0.37\text{-}\lambda$  dipole antennas made of *Nb* whose mixing elements are *Nb/Al-Al<sub>2</sub>O<sub>3</sub>/Nb* SIS (superconductor-insulator-superconductor) devices of  $3\mu\text{m}\times 3\mu\text{m}$  size and  $5\text{kA}/\text{cm}^2$  critical current density. The result of the heterodyne mixing of the local oscillator and the black body signal is a 1.5 GHz signal which is extracted and amplified. The design is such that the sensors operate in the vicinity of 190 GHz. The dipole antennas are fabricated on a  $1\text{-}\mu\text{m}$  thick silicon nitride membrane embedded in a micromachined cavity. The pyramidal cavity is formed by anisotropic etching of silicon wafers. A machined section is placed next to the micromachined one to improve the coupling efficiency of the detector. I-V, noise, FTS (Fourier Transform Spectroscopy), beam pattern measurements are conducted to unveil various features of the imaging array. Finally, an initial stage which explores experimentally the integration of local oscillators based on the Josephson effect is presented.

Light weight, compactness, and ease of fabrication are some of the important features of this array of receivers. The lowest noise temperature range across the array elements was measured to be 62 K - 102 K and the bandwidth 40 GHz for 2.7 K bath temperature. The uniformity and satisfactory operation of the receivers make the idea of the array attractive for imaging applications.

Thesis Supervisor: Qing Hu

Title: Associate Professor of Electrical Engineering and Computer Science





## **Acknowledgments**

I would like to thank my Professor Qing Hu for giving me the opportunity to cross the Atlantic and explore the New World of MIT and for guiding me through this ambitious project. Group 86 of MIT Lincoln Laboratories and Hypres Inc are acknowledged for their contribution in the fabrication process.

I consider myself lucky to work with other colleagues who became my tutors and friends during the past two years, Arifur Rahman, Ben Williams, Bin Xu, Brian Riely, Erik Duerr, Farhan Rana, Ilya Lyubomirsky and Noah Zamdmer. I would like to thank our postdoc Gert de Lange who was the soul of this research project and my patient teacher. My close friends and my family back home were my true inspiration and support, reminding me of little things in life that make it so great.

This work was supported by the National Science Foundation under grant No. 9423608-AST, and by NASA under grant No. NAGW-4691.



# Contents

<b>1</b>	<b>Introduction</b>	<b>11</b>
1.1	Motivation . . . . .	11
1.2	Approach . . . . .	13
1.3	Thesis Overview . . . . .	15
<b>2</b>	<b>Theory and Design</b>	<b>17</b>
2.1	Theory of SIS Junctions . . . . .	17
2.1.1	General Characteristics . . . . .	17
2.1.2	Types of Detection . . . . .	19
2.1.3	Local Oscillator Based on the Josephson Effect . . . . .	23
2.2	Design Issues . . . . .	24
2.2.1	Geometry of Horn and Antenna . . . . .	24
2.2.2	Tuning Elements and Impedance Transformation Issues . . . . .	26
2.2.3	RF capacitor/ DC-IF board/ Magnet . . . . .	28
2.2.4	LO Design Issues . . . . .	30
2.2.5	Optics . . . . .	33
<b>3</b>	<b>Fabrication Steps and Preparation of the Experimental Set-Up</b>	<b>35</b>
3.1	Fabrication Steps . . . . .	35
3.1.1	Device Wafer Fabrication . . . . .	36
3.1.2	Micromachining Process . . . . .	39
3.1.3	Gold Deposition . . . . .	41
3.2	Preparation of the Experimental Set-Up . . . . .	42

3.2.1	Mounting Process of the Wafers . . . . .	42
3.2.2	Preparation of the Experimental Set-Up on the Cold Plate of the Dewar . . . . .	44
3.2.3	Description of the Cryogenic Unit . . . . .	46
3.2.4	Biasing Circuitry . . . . .	47
<b>4</b>	<b>Measurements</b>	<b>51</b>
4.1	Array Unpumped I-V Characteristics . . . . .	51
4.2	Noise Measurements . . . . .	52
4.2.1	Experimental Set-Up and Measurements . . . . .	54
4.3	Beam Pattern Measurements . . . . .	59
4.3.1	Experimental Set-Up and Measurements . . . . .	59
4.4	Fourier Transform Spectroscopy (FTS) Measurements . . . . .	61
4.4.1	Experimental Set-Up and Measurements . . . . .	62
4.5	Josephson Junction Local Oscillator (JJLO) Measurement . . . . .	63
<b>5</b>	<b>Conclusions - Future Work</b>	<b>65</b>
5.1	Conclusions . . . . .	65
5.2	Future Work . . . . .	65
<b>A</b>	<b>Biasing Circuitry</b>	<b>67</b>

# List of Figures

1-1	<i>Cross section of the detector.</i>	13
2-1	<i>SIS junction energy diagram.</i>	18
2-2	<i>Typical I-V characteristic of SIS junction.</i>	19
2-3	<i>Block diagram of a heterodyne mixer.</i>	20
2-4	<i>Simplified circuit description of heterodyne mixing.</i>	21
2-5	<i><math>P_{IF}</math> at the first photon step.</i>	23
2-6	<i>Geometry of the machined/micromachined section.</i>	25
2-7	<i>Integrated tuning structure: (a) planar geometry, (b) equivalent circuit.</i>	27
2-8	<i>Selection of a particular design: (a) device wafer with four different designs, (b) top wafer.</i>	28
2-9	<i>RF choke capacitor: (a) planar geometry, (b) equivalent circuit.</i>	29
2-10	<i>A unit of the DC-IF board: (a) planar geometry, (b) equivalent circuit.</i>	29
2-11	<i>Expanded view of the array receiver.</i>	31
2-12	<i>Planar picture of the receiver with the LO.</i>	32
2-13	<i>Detail of tuning and coupling structures.</i>	32
2-14	<i>Circuit equivalent of the antenna with LO line and current control line.</i>	32
2-15	<i>Optical scheme of the imaging array.</i>	34
3-1	<i>Cross section of a typical Hypres wafer.</i>	37
3-2	<i>Junction definition: (a) Trilayer deposition and base electrode definition; (b) junction definition; (c) <math>\text{SiO}_2</math> deposition and patterning; (d) wiring deposition and patterning.</i>	39
3-3	<i>Micromachining steps</i>	40
3-4	<i>Top schematic of the cold plate.</i>	46
3-5	<i>Cryogenic Unit.</i>	47
3-6	<i>Block diagram of a biasing unit.</i>	48
4-1	<i>Unpumped I-V characteristics across the imaging array.</i>	52
4-2	<i>(a) Definition of noise temperature, (b) noise temperature chain rule.</i>	53
4-3	<i>Experimental set-up for heterodyne measurements.</i>	54
4-4	<i>I-V pumped characteristics and <math>P_{IF}</math>-V for hot-cold load across the array.</i>	57
4-5	<i>Noise temperature vs frequency across the array.</i>	58
4-6	<i>Experimental set-up for beam pattern measurements.</i>	59
4-7	<i>Beam pattern measurements of elements #5 (center) and #4 (off-axis).</i>	60
4-8	<i>Experimental set-up for FTS measurements.</i>	62

4-9	<i>FTS measurement of the 140 <math>\mu\text{m}</math> - 190 <math>\mu\text{m}</math> design.</i>	63
4-10	<i>Detail of the stick used for dip-stick measurements.</i>	64
4-11	<i>Pumped and unpumped characteristic with integrated JJLO.</i>	64

# Chapter 1

## Introduction

### 1.1 Motivation

The millimeter wave frequency range (30-300 GHz) has been extensively investigated by many researchers in the last two decades for a variety of applications. An attractive feature of this region when compared with the microwave one is that higher resolution can be achieved because of the shorter wavelength. This also results in more compact and lighter devices. The microwave region has been widely used in the past and the demand for alternative frequency windows has boosted the interest for higher frequencies and larger bandwidths. The optical and infrared region seems to be a better choice but the major drawback is its poor transmission in situations of fog, dust, and inclement weather ([1],[2]). Under these conditions the millimeter waves have unparalleled superiority. From this perspective, there are several military applications taking advantage of these features (weapon detection, aircraft landing systems) ([3],[4]). Furthermore, a rise of commercial applications in the millimeter wave region is notable, mainly in the area of communications and radars (PCN, collision avoidance radars) ([5],[6]).

The atmosphere is characterized by many frequency windows in the millimeter wave region. Millimeter and submillimeter spectral lines observed in galaxies have their origin in rotational transitions of molecules ( $SO$ ,  $CO$ ) residing in interstellar or circumstellar gas clouds ([7]). Thus, the millimeter wave region is attractive for radioastronomical applications. Moreover, remote sensing to monitor air pollutants can be facilitated as well

as remote sensing of the ozone cycle and other atmospheric chemistry ([8]).

Another area of interest is plasma diagnostics. A detailed knowledge of collective behavior of plasmas is important for successful fusion power. Sensitive millimeter wave detectors are useful for this purpose ([9], [10]).

SIS devices as sensors in the millimeter wave range serve satisfactorily most of the above applications. The most attractive feature of SIS is that according to the quantum mechanical mixing theory in quasiparticle tunnel junctions the mixer noise temperature can approach the quantum limit ([11]). Thus, the sensor is very sensitive to low-power signals of the millimeter wave range. Furthermore, SIS mixers are not limited by conversion loss which characterizes classical resistive mixers. In fact, they achieve large conversion gain and thus decrease the IF amplifier's contribution to the total system noise ([12]).

Fabrication of small-dimension millimeter wave structures using the standard microwave technology can be costly. The idea of micromachining solves this problem since the well known technology of silicon can be applied ([13]). Moreover, the mature hybrid and monolithic technology can be used for the fabrication of dipole antennas and SIS sensors, promoting the idea of compactness in this frequency regime. Anisotropic etching of silicon is applied to form a pyramidal cavity made of a stack of wafers. The dipole antenna is fabricated on a silicon nitride membrane which practically does not cause any attenuation ([14]). Because of the wide flare angle of  $70.6^\circ$ , the gain achieved is low. One solution for optimizing the coupling of incoming waves to the detector is the use of a machined pyramidal cavity on top of the micromachined antenna.

Since the fabrication process can be applied with nearly the same cost on a large area, the idea of an array of detectors can be easily materialized. Applications include imaging and significant reduction of observation time for radioastronomy by a factor of  $N$ , where  $N$  is the number of sensors ([15],[16]). The mechanical scan of the sensors is significantly reduced. In addition, the imaging achieved is passive which is attractive in terms of power consumption.

The array of sensors has plenty of space for extra integrated circuitry including local oscillators and IF amplifiers. Hence, all the basic units of the mixer could be fabricated monolithically, minimizing the cost for extra devices inside and outside the cryogenic unit.



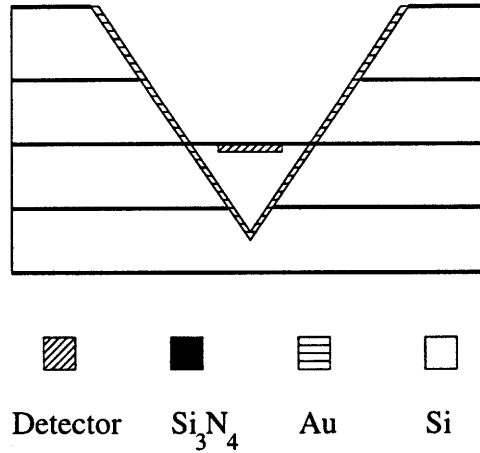


Figure 1-1: *Cross section of the detector.*

## 1.2 Approach

This research project focuses on a 3x3 array of  $0.37\text{-}\lambda$  dipole antennas that use SIS devices as mixing elements. The frequency of interest is in the region of 190 GHz. The antennas are fabricated on a silicon nitride membrane deposited on a silicon wafer. The device wafer is stacked with two backing wafers and one aperture wafer (Figure 1-1). The number of wafers used is such that the desired geometrical characteristics of the cavity are implemented given the thickness of silicon wafers available in the market. The optimum dimensions of the antenna and the cavity have been discussed in [17]. The choice of the center frequency was fixed by the experimental set-up. A Gunn oscillator operating in the region of 95 GHz is connected to a doubler to provide maximum power in the region of 190 GHz. Members of my research group have been working with microbolometers and SIS devices in the region of 95 GHz so the next step for higher frequencies was the second harmonic. It is unfortunate that water vapor has a strong absorption line at 183.3 GHz ([18]). Frequency windows that don't suffer significant attenuation by water vapor or  $\text{CO}_2$  open up at 35 GHz, 94 GHz, 140 GHz, 220 GHz, 340 GHz, 410 GHz. Currently, the 200 GHz band is being used for radio astronomy and for monitoring concentrations of atmospheric constituents such as  $\text{ClO}$  which plays a significant role in the depletion of ozone layer ([8]).

The SIS devices used are made of  $\text{Nb}$  whose fabrication technology is mature and reliable. In order to achieve better coupling of the radiation received by the antenna to the mixer, an integrated tuning structure has been used ([19], [20]). In that way, proper

impedance transformations ensure maximum transfer of 190 GHz radiation to the SIS device.

Local oscillators using the Josephson effect have been a research issue for many years ([21]). Their integration on the device wafer where the SIS mixers are fabricated promotes compactness, thus making unnecessary the use of an external Gunn oscillator. Furthermore, the difficult problem of directing the power of the Gunn oscillator to the devices with the use of a beamsplitter can be avoided. In addition, the noise performance is optimized since the contribution of the beamsplitter as a 300 K black body is not involved in the chain of devices. HYPRES Inc has been analysing a series of resistively shunted Josephson junctions to achieve a satisfactory power level in the frequency region of 190 GHz. This design has been combined with a simple coupling scheme to provide LO power to the SIS mixer.

This main aim of this project is to verify low noise receiver temperature which is comparable with receiver temperature of other research groups employing other or similar approaches ([22],[23],[24]). The best reported result of SIS devices until now in this frequency region is 45 K ([22]). In addition, uniformity of characteristics among the elements of the array is another important issue since it will make the idea of an array more attractive. Finally, a satisfactory operation of integrated local oscillators combined with the current design is another issue of interest.

The fabrication of the device wafer is conducted at HYPRES Inc. In addition, the micromachining of the device wafer is performed there. At MIT Lincoln Laboratories we micromachined the backing wafers and the aperture wafers, aligned and stacked the wafers. For testing purposes, designs of different center frequencies have been implemented so many stacks of wafers have been prepared.

Measurements will focus on I-V characteristics with (pumped) and without (unpumped) external radiation, IF (Intermediate Frequency) power vs V, FTS (Fourier Transform Spectroscopy) and beam patterns. I-V characteristics show the quality of the SIS junctions and the degree of external radiation coupling. IF power peak at the first photon step is used to find the noise performance of the receiver when hot (300 K) and cold (77 K) loads are placed in front of the window of the cryogenic unit. Furthermore, a good characteristic of a receiver

is the broad bandwidth around the designed frequency. Hence, different frequencies can be tested for their noise performance. In terms of coupling, FTS measurements provide information in the frequency regime. Finally, beam pattern measurements can show the gaussian properties of the detectors across the array.

### **1.3 Thesis Overview**

The theory of SIS mixers and the design issues involved will be presented in chapter 2. The fabrication process along with the preparation of the experimental set-up will be discussed in chapter 3. The measurements will be presented and analysed in chapter 4. Finally, chapter 5 will be devoted to the conclusions drawn and the future work of this research.



# Chapter 2

## Theory and Design

An efficient receiver must be equipped with a sensitive solid-state device that is placed in a well-designed electromagnetic environment. The designer must understand the operation of the device and choose the optimum coupling scheme that fits its requirements. The following discussion will present some theoretical issues of the SIS device and the microwave design of the receiver.

### 2.1 Theory of SIS Junctions

The theory of superconductivity is elegant as well as complicated since it lies heavily on many-body theory. The monumental work of J. Bardeen, L. N. Cooper and J. R. Schrieffer on the interpretation of superconductivity resulted in the nobel-prized BCS theory ([25]). I would not try to get into the essence of this approach. I will briefly mention some basic results of the operation of SIS devices which are mainly presented in [7], [26]. The interested reader is urged to read the above for more details in a less formal approach than BCS theory.

#### 2.1.1 General Characteristics

In metals above a temperature, known as critical temperature  $T_c$ , the electrons move randomly because of thermal agitation. Below  $T_c$ , the metal no longer behaves as normal.

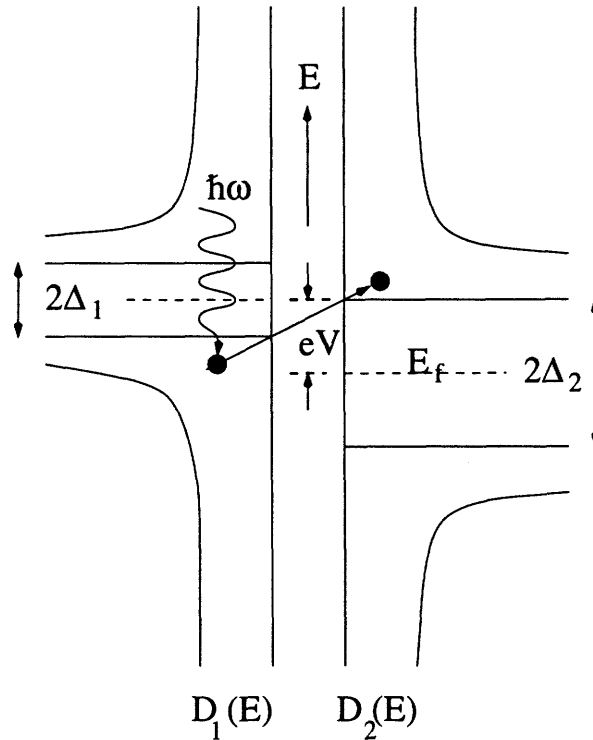


Figure 2-1: SIS junction energy diagram.

The superconductive state is characterized by the collective motion of electrons which form pairs, the so-called Cooper pairs. These pairs are formed by electron-phonon interaction which results in a weak attraction between the electrons. The minimum energy to break the Cooper pair into two so-called quasiparticles is  $2\Delta$ , where  $\Delta$  is the energy for one quasiparticle excitation. The superconductive state of all the Cooper pairs can be represented by a single wavefunction  $\Psi$ .

The SIS device consists of two superconductors separated by a thin insulating layer which allows quantum mechanical tunneling of Cooper pairs and quasiparticles. When the bias voltage is  $|V| < \frac{\Delta_1 + \Delta_2}{e}$ , no current flows since there is not enough energy to break Cooper pairs. When  $|V| > \frac{\Delta_1 + \Delta_2}{e}$ , Cooper pairs break and the quasiparticles tunnel through giving rise to current following an almost linear characteristic of a normal metal. A simple picture to describe the behavior of a superconductor, especially when it is part of a junction, is given by the 'semiconductor model'. The energy gap in this semiconductor approach is  $2\Delta$ , the valence band accounts for the 'quasiholes' and the conduction band accounts for the 'quasielectrons'. Each band is described by its respective density of states,

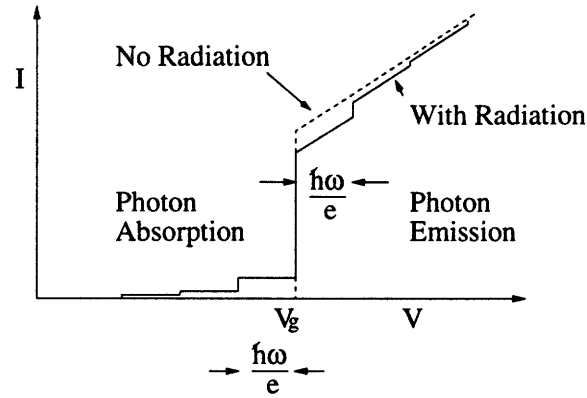


Figure 2-2: Typical I-V characteristic of SIS junction.

$$D(E) \propto \frac{E}{\sqrt{E^2 - \Delta^2}}.$$

An important feature of the SIS device appears when external radiation is applied, leading to a step structure of the I-V characteristic. The absorption of  $n$  quanta inside the barrier is sufficient to cause quasiparticle tunneling when  $|eV| + n\hbar\omega > \Delta_1 + \Delta_2$  (Figure 2-1). In the same fashion, emission is possible and for this case  $n$  is a negative integer. We will see shortly that our interest is on the first photon step where absorption of a photon takes place. This has to do with the fact that it is close to the I-V nonlinearity at the gap voltage (Figure 2-2).

Apart from the single-particle current, Cooper pair tunneling is also possible giving rise to the so-called supercurrent. BCS theory has derived the maximum value of this DC current for zero applied voltage to be  $I_c = \frac{\pi}{4} \frac{V_g}{R_n}$ , where  $R_n$  is the normal state resistance. The suppression of the supercurrent can be achieved with the application of external magnetic field.

### 2.1.2 Types of Detection

The SIS devices can operate in two different modes, direct (or video) detection and heterodyne detection.

When direct detection is considered, incoming photons are converted into DC current. SIS devices can reach the quantum limit where every photon causes tunneling of an electron. Information of phase is lost, only the power level and the frequency of the incident radiation can be extracted from the I-V curve. The leakage current of the junction determines the noise

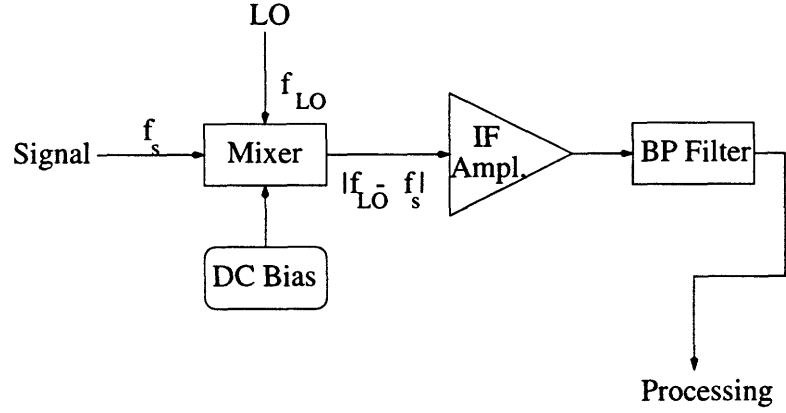


Figure 2-3: Block diagram of a heterodyne mixer.

(here, shot noise) of the detector.

Most of the applications of SIS junctions stem from the heterodyne detection (Figure 2-3). Incoming radiation of frequency  $f_s$  is combined with a local oscillator signal of frequency  $f_{LO}$ . The SIS device acts as a mixer, producing a signal of the intermediate frequency (IF)  $|f_{LO} - f_s|$ . In this mode of operation, the information of power level, phase and frequency of the signal can be extracted from the IF signal. Furthermore, no extra noise is added, only the zero point noise of the incoming radiation is amplified by the mixer gain.

### Direct Detection

If we represent the external radiation by an additive sinusoidal term to the DC bias point, the quasiparticle energy level of interest is split into discrete energy levels of  $\hbar\omega$  separation. The external radiation leads to a different DC I-V characteristic as well as to the creation of a current component of the same frequency. Both are contributing to the current responsivity which is defined as :

$$R_i \equiv \frac{\Delta I_{dc}}{\frac{1}{2}V_\omega I_\omega}. \quad (2.1)$$

Following the derivation of [26], we can prove quantum mechanically that

$$R_i = \frac{e}{\hbar\omega} \frac{I_{dc}(V_0 + \hbar\omega/e) - 2I_{dc}(V_0) + I_{dc}(V_0 - \hbar\omega/e)}{I_{dc}(V_0 + \hbar\omega/e) - I_{dc}(V_0 - \hbar\omega/e)} \quad (2.2)$$



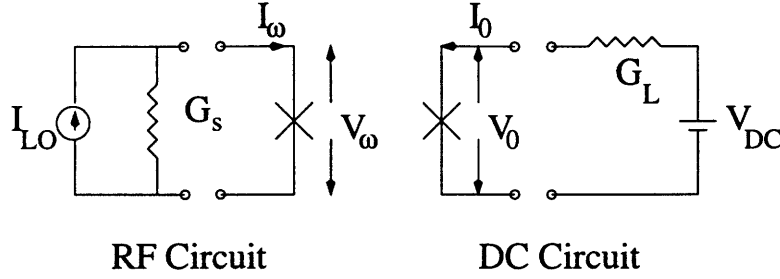


Figure 2-4: *Simplified circuit description of heterodyne mixing.*

where  $V_0$  is the DC bias voltage. When we are dealing with low frequencies, the above expression leads to the classical result:

$$R_i \rightarrow \frac{1}{2} \frac{d^2 I_{dc}/dV_0^2}{dI_{dc}/dV_0}, \quad \hbar\omega \ll e|V_0|. \quad (2.3)$$

Thus, a classical mixer does not have an upper limit of responsivity. So, by increasing the curvature of the nonlinearity we could get a significant responsivity. This cannot be verified experimentally. The quantum mechanical limit of the current responsivity is

$$R_i \rightarrow \frac{e}{\hbar\omega}, \quad \hbar\omega \simeq e|V_0|. \quad (2.4)$$

This can happen when a single photon is sufficient to make a quasiparticle tunnel through the barrier. We could expect that if the nonlinearity starts at  $V_0$  and  $I_{dc}(V_0 + \hbar\omega/e)$  is much higher than the rest of the terms, quantum limit is almost reached. Thus, the first photon step is the region of interest. The detailed description of the DC curve is sufficient to describe the interaction with external radiation.

## Heterodyne Detection

The phenomenological theory of mixing described in [26] lies on the simplification that the IF signal is of low frequency that can be treated as DC signal. Consequently, the LO and the signal are considered to have the same frequency.

In terms of circuit representation, Figure 2-4 illustrates the above. The figure of merit

used is the conversion gain which is also called inverse conversion loss. It is defined as

$$L^{-1} \equiv \frac{P_{IF}}{P_{sig}}. \quad (2.5)$$

The IF signal is derived as the differential signal of  $I_{DC}$  and the RF signal as the differential of  $I_{LO}$ , with  $V_{dc}$  held constant in both cases. If we define

$$G_{ij} \equiv \frac{\partial I_i}{\partial V_j} \quad (2.6)$$

where  $i, j \equiv 0, \omega$ , the maximum conversion gain can be proven to be

$$L_{avail}^{-1}(V_{dc}, P_{LO}, G_s) = \begin{cases} L_0^{-1} \frac{\eta g_s}{(1+g_s)(1+g_s-\eta)}, & 1 + g_s > \eta \\ \infty, & 1 + g_s \leq \eta \end{cases} \quad (2.7)$$

where  $L_0 \equiv \frac{G_{\omega 0}}{G_{0\omega}}$ ,  $\eta \equiv \frac{G_{0\omega} G_{\omega 0}}{G_{00} G_{\omega\omega}}$  and  $g_s \equiv \frac{G_s}{G_{\omega\omega}}$ . The factor  $\eta$  is characteristic of the device of interest and embodies its nonlinearity. For a classical mixer, where the current changes instantaneously with voltage, it is found that  $L_0^{-1} = L_{max}^{-1} = 0.5$  and this is achieved for  $\eta = 1$ . Thus, the mixer does not show actual gain.

The quasiparticle mixer behavior comes into play when we are dealing with high enough frequencies so that the assumption of instantaneous change of current with voltage fails. In this case,  $L_0^{-1}$  can be greater than unity leading to a net conversion gain

$$L^{-1} \approx L_0^{-1} \frac{4g_s}{1+g_s} \frac{1}{g_L} \quad (2.8)$$

where  $g_L \equiv \frac{G_L}{G_{00}}$ . Hence, the conversion gain becomes proportional to the applied load. This behavior is typical of a current source. Furthermore, it is possible to get  $\eta > 1$  which can happen when the pumped characteristic shows a negative impedance region. Working in the negative differential region can lead to instabilities as explained in [26]. In general, the SIS device is designed to operate in a positive differential impedance region with a sufficient conversion gain.

It is not straightforward to relate the conversion gain with the noise temperature performance of the receiver since it demands strict quantum mechanical formulation. A simplified

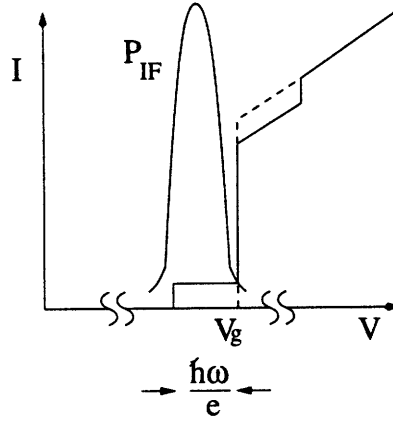


Figure 2-5:  $P_{IF}$  at the first photon step.

explanation is presented in [26]. For practical cases, whenever we have a satisfactory conversion gain, the shot noise of the receiver is low.

A typical I-V characteristic with  $P_{IF}$  is shown in Figure 2-5

### 2.1.3 Local Oscillator Based on the Josephson Effect

A brief introduction of the Josephson effect for LO signal is attempted here. The simple picture given below, is mainly derived from Hypres Inc reports.

SIS junctions can be used as voltage-controlled oscillators. The basic equations governing the Josephson effect are:

$$I = I_j \sin(\Phi) \quad (2.9)$$

$$\frac{d\Phi}{dt} = \frac{2\pi V}{\Phi_0} \quad (2.10)$$

where  $\Phi_0 = 2.07\text{pH-mA}$  the flux quantum,  $I$  the Josephson current flowing the tunnel junction,  $V$  the applied voltage and  $\Phi$  the phase drop across the junction. These equations show that an oscillating current of voltage-controlled frequency will be generated.

An inherent disadvantage of this type of LO is the low power, low impedance and broad linewidth of a single junction. If an array of phased-locked LO is used, the generated power will be multiplied by the number of junctions. The available power from such an array to a matched load is proven to be

$$P_{avail} = \frac{I_c^2 N R_j}{8} \quad (2.11)$$

where  $I_c$  is the critical current and  $R_J$  the junction shunt resistance.

The linewidth of the radiation emitted by a single Josephson junction is proven to be 40 MHz/K- $\Omega$ . For an array, the linewidth is reduced by a factor of 1/N for N junctions.

## 2.2 Design Issues

The fundamental issues that concern the RF designer can be summarized to the following: geometry of the coupling structure, efficient operation of the solid-state device when placed in the coupling structure, separation of the various frequency channels (RF, IF, LO, DC), satisfactory optical scheme. The discussion that follows will address these questions and present the design solution.

### 2.2.1 Geometry of Horn and Antenna

In general, the device used for electromagnetic detection must be accompanied by a satisfactory coupling structure so that the potential of the detector is fully exploited. Figures of merit commonly used, ([27]) are:

- coupling efficiency
- cross polarization levels
- gain
- directivity.

Extensive research has been conducted in micromachined horn antennas by the University of Michigan ([28], [29], [30], [31]).

An electromagnetic cavity is formed by a stack of micromachined wafers. Micromachining is performed by anisotropic etching of silicon wafers: KOH etches the  $\langle 100 \rangle$  face faster than  $\langle 111 \rangle$  forming a pyramidal cavity of  $70^\circ$  flare angle.

The antenna is fabricated on a  $Si_3N_4$  membrane which is embedded in the micromachined cavity. This type of membrane is selected because it is characterized by a low power

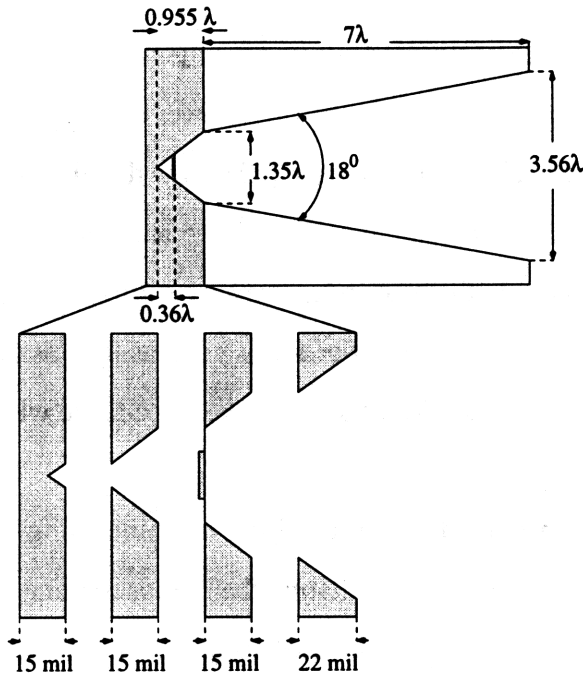


Figure 2-6: *Geometry of the machined/micromachined section.*

dissipation and a notable mechanical strength. Thus, the antenna is standing practically in the free space. A simple  $0.37\text{-}\lambda$  dipole antenna is used.

The inherent disadvantage of this design is the wide flare angle leading to an antenna gain less than 13 db and the 10-db beamwidth larger than  $90^\circ$ . A machined small flare-angle pyramidal section, placed next to the micromachined cavity proved to be a good coupling structure. This extra section acts as a mode converter. The main contribution comes from  $TE_{10}$ ,  $TE_{12}$ ,  $TM_{12}$ ,  $TE_{30}$  and their interference depends on the particular geometry. The far-field patterns are circularly symmetric and the cross-polarization is sufficiently low. The design chosen for this project is theoretically proven to have the following features:

- 20 db antenna gain
- $34^\circ$  10-db beamwidth
- -27 db sidelobe level (E-plane)
- -22.7 db cross polarization level.

The various parameters of the pyramidal cavity are shown in Figure 2-6 in units of the designed center wavelength of operation. For the 190 GHz design, the theoretical geometry

is approximated by a stack of two backing wafers, the device wafer and a top aperture wafer.

An important design issue for coupling RF power to the SIS detector is the impedance seen from the antenna leads. Simulations in [17] show that the impedance is approximately  $50 \Omega$ . Having this in mind, we could substitute the antenna and the cavity with a resistor, right at the antenna leads. In that way, microwave coupling issues become less complicated. A word of caution though; this simplification is valid as long as the frequency of operation is close to the designed frequency. Otherwise, the impedance will be frequency-dependent and not purely resistive.

The machined horn is made with a milling machine using the split-block technique. High packing density is achieved, facilitating the purpose of imaging. The array is made of six gold-plated tellurium copper blocks and fabricated at Lincoln Lab.

### **2.2.2 Tuning Elements and Impedance Transformation Issues**

For a maximum transfer of RF power to the SIS junction, the geometrical capacitance must be tuned out at the operation frequency. A technique that has been successfully used in [19], [20], [7], [32] is the integrated tuning structure. The antenna structure that we use has planar geometry. The dipole itself consists of two Nb strips of finite width. The feeding circuit is two coplanar Nb strips which are connected to the antenna pads. If we place dielectric and a thin metallic strip in the center and along the above wide microwave structures, the perturbation will be small and to a first degree, can be ignored. Thus, one of the coplanar Nb strips can be utilized as the ground plane of a microstrip structure. This ground plane is connected to the base electrode of the SIS (the first 'S'). Likewise for the top plane and the counterelectrode (the second 'S'). This microstrip starts from the antenna leads so that the antenna impedance can be conveniently placed there for the design calculations.

The choice of the SIS geometry was restricted by the design rules imposed by our wafer supplier, Hypres Inc. The minimum size of the junction is limited to  $3\mu m \times 3\mu m$ , the capacitance is  $38 \text{ fF}/\mu m^2$  for a dielectric with  $\epsilon_r = 5.4$  and thickness  $0.2 \mu m$ . The critical current density for this batch of devices was  $5 \text{ kA}/\text{cm}^2$ . Given the above, the normal resistance of the SIS junction is calculated to be approximately  $5 \Omega$  and the capacitance

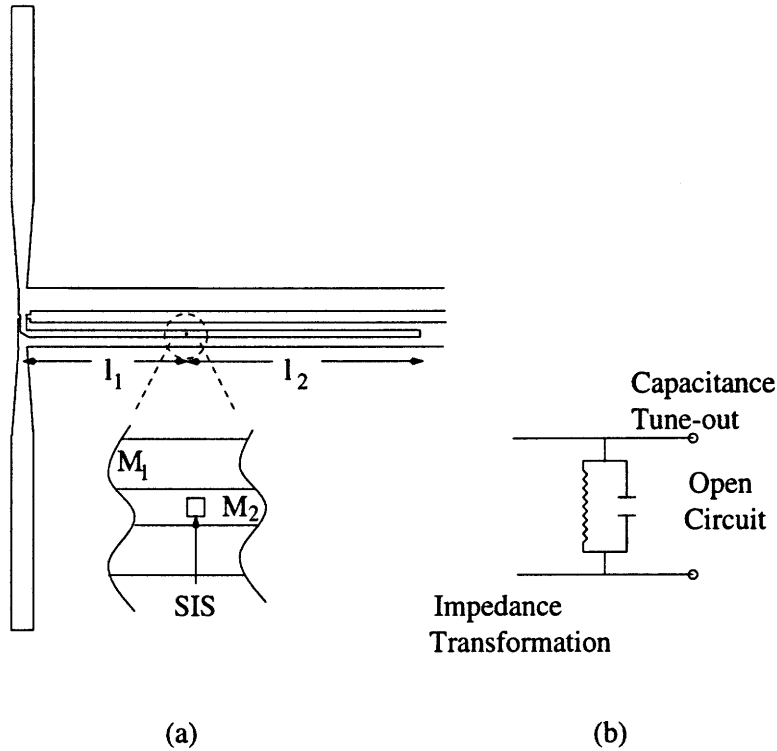


Figure 2-7: *Integrated tuning structure: (a) planar geometry, (b) equivalent circuit.*

0.342 pF. Since the antenna impedance is  $50 \Omega$ , we can expect a significant impedance mismatch. Thus, two issues have to be resolved: first, the capacitance must be tuned out, and second, the SIS impedance must be transformed to the antenna impedance.

To tune out the capacitance, an open-ended tuning structure is used and the impedance transformation is achieved by a second microstrip (Figure 2-7). The impedance seen at the end of the microstrip is  $\infty$  and after  $\lambda_{RF}/4$  it is transformed to short circuit. By choosing a microstrip a bit longer than  $\lambda_{RF}/4$ , the microstrip seen by the SIS is inductive. Thus, the capacitance can be tuned out. The second microstrip is chosen to transform the low impedance to the required  $50 \Omega$ .

The above calculation has to be made in the context of superconductive properties where skin effects are important. A detailed analysis on the calculation of parameters involved in determining the characteristic impedance of a superconductive microstrip can be found in [7], [33].

We must take into consideration the following issues in the design: a) the external Gunn oscillator has a narrow bandwidth, b) the antenna impedance is frequency-dependent, c)

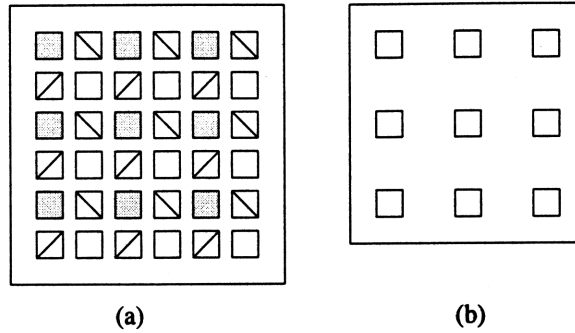


Figure 2-8: *Selection of a particular design: (a) device wafer with four different designs, (b) top wafer.*

the fabrication process has some error margins for the length of the microstrips, d) there may be a dispersion of fabricated SIS areas as well as current densities, e) the best noise performance does not coincide with the optimum gain performance. That's why for this batch different lengths of microstrips were tested. We named the devices according to the length of the first and second microstrip in  $\mu m$ . The designs implemented are: 155 - 190 (165 GHz), 145 - 190 (174 GHz), 140 - 190 (178 GHz), 135 - 160 (188 GHz), 130 - 160 (193 GHz), 125 - 160 (198 GHz), 120 - 140 (208 GHz), 110 - 140 (222 GHz).

Gerhard de Lange came up with a very handy way to implement the following designs on chip. Every device wafer hosts 6x6 antennas of 4 different designs. The top wafer is the one that selects the devices of interest. Figure 2-8 illustrates the above.

### 2.2.3 RF capacitor/ DC-IF board/ Magnet

The generated IF signal from the SIS mixer must be directed to the external IF amplifier. It travels towards the antenna pads via the coplanar strips. The problem that we face is that the DC bias must follow the same path and the IF signal must not be lost at the DC bias connection. Furthermore, the RF power must be directed to the microstrip tuning structure and not the coplanar strips. The latter is solved with the fabrication of a RF choke capacitor and the former with a T-circuit which is implemented with a DC-IF board.

The RF choke is formed by a layer of metal below the coplanar feeding strips at a distance  $\lambda_{RF}/4$  from the dipole antenna (Figure 2-9). For the RF signal, the capacitor behaves like a short circuit. This is transformed into an open circuit at the antenna. Thus, the RF



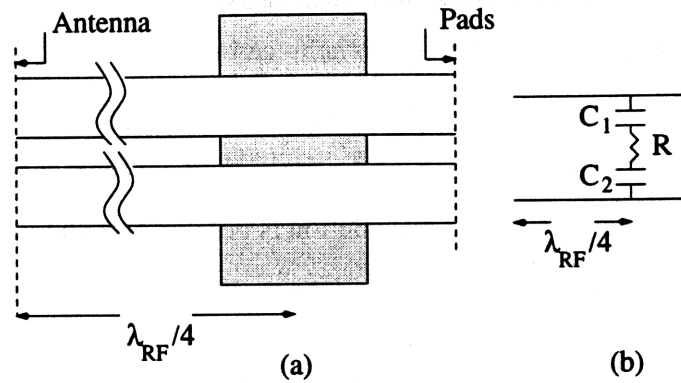


Figure 2-9: RF choke capacitor: (a) planar geometry, (b) equivalent circuit.

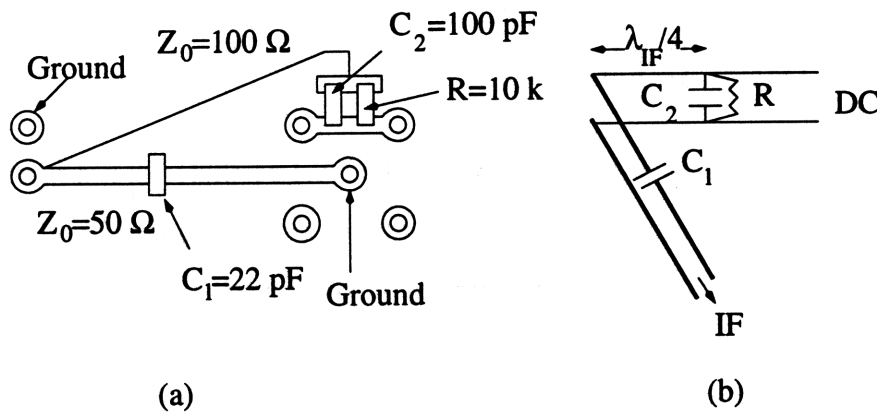


Figure 2-10: A unit of the DC-IF board: (a) planar geometry, (b) equivalent circuit.

signal will be highly reflected in this path and guided to the integrated tuning structure. We should point out that there is some length ambiguity since it is hard to tell where we should measure the  $\lambda_{RF}/4$  distance due to the finite size of the capacitor plate. It turned out that this is not very critical for the measured noise performance. Even without the RF choke capacitor (which occurred as a fabrication error), good results were measured because of the impedance mismatch between the planar structure of the pads and the coplanar strips.

The DC-IF board is connected to the antenna pads. It was designed by Gerhard de Lange and fabricated at Lincoln Lab. It is made of Duroid 6010 material. One side (ground) is coated with Au, while the microstrips are printed on the other side which is shown in Figure 2-10. The chip capacitors  $C_1$ ,  $C_2$  are virtually shorted for the IF signal and open for the DC signal. Thus, the path containing  $C_1$  is permitted for the IF but blocked for the DC signal.  $C_2$  is transformed into an open circuit at a distance  $\lambda_{IF}/4$ , so the IF signal is blocked while the DC signal can pass. The chip resistor  $R$  is used to avoid any charge built-up.

The suppression of Josephson effects is achieved with a magnet placed between the DC–IF board and the backing wafer. A copper coil is used with approximately 2500 turns of Nb wire (Supercon T48B). The direction of the magnetic field (perpendicular to the junction) is not optimum. However, the field distribution is not uniform and a tangential component of the magnetic field can be produced. Hence, the Josephson current is satisfactorily suppressed.

Figure 2-11 illustrates the various parts of the receiver discussed so far.

## 2.2.4 LO Design Issues

Here, we will not try to get into the design of the local oscillator. It is a rather complicated research project of Hypres Inc. Let's take for granted that LO signal of the desired frequency is generated. We wish to couple this signal to the SIS junction. The coupling must be such that no significant RF signal is lost at the LO structure. The LO signal reaching the junction must not be weak, otherwise no photon steps will be observed. On the other hand, it should not saturate the device. Hypres Inc has reported output power in excess of  $3.5 \mu W$  at 120 GHz using a  $60 \Omega$  load.

Another degree of complication is added by the introduction of a control line for the suppression of Josephson effect. Replacing the magnet, a Nb strip supplied with DC current and passing over the SIS, creates the desired magnetic field. This extra line must not affect the integrated tuning structure or the LO line.

The actual receiver is illustrated in Figure 2-12 and the various microstrips involved in tuning and coupling are shown in Figure 2-13. A simplified schematic is shown in Figure 2-14 with the various metallic layers ( $M_{2t}$  stands for  $M_2$  layer used for impedance transformation,  $M_{2c}$  stands for  $M_2$  layer used for coplanar feeds). The lengths  $l_1$ ,  $l_2$  are selected in the way we described earlier. The pieces of  $M_{2t}$  of length  $l_3$  and  $l_4$  are not connected with each other. If we assume that they are practically connected due to the capacitive coupling, then if lengths  $\lambda_{RF}/4$  are chosen, the integrated tuning structure will not be affected. If one wants to be precise, the microstrip discontinuities must be carefully modelled with equivalent circuits. Given the limited time frame of this research, no actual

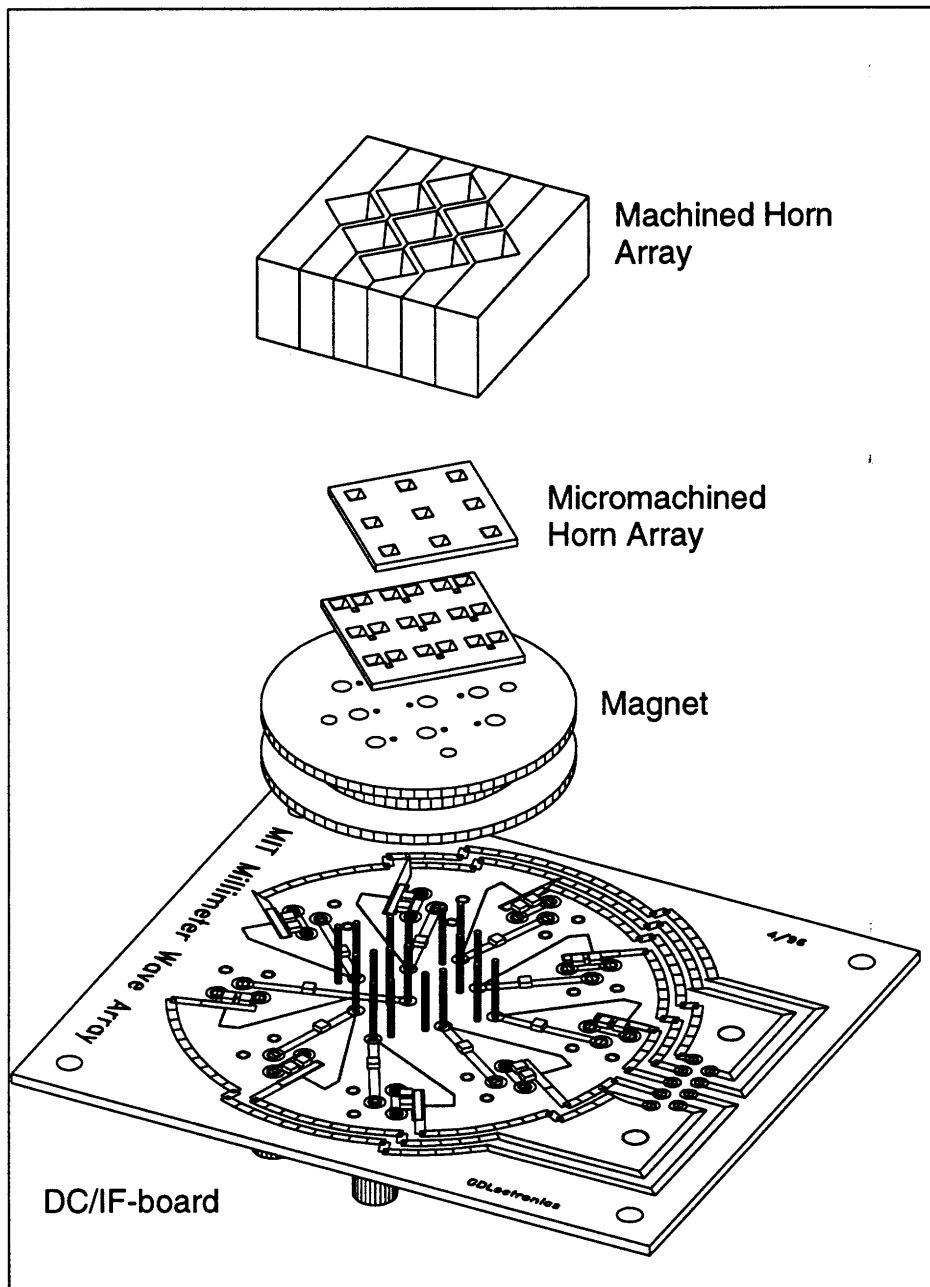


Figure 2-11: Expanded view of the array receiver.

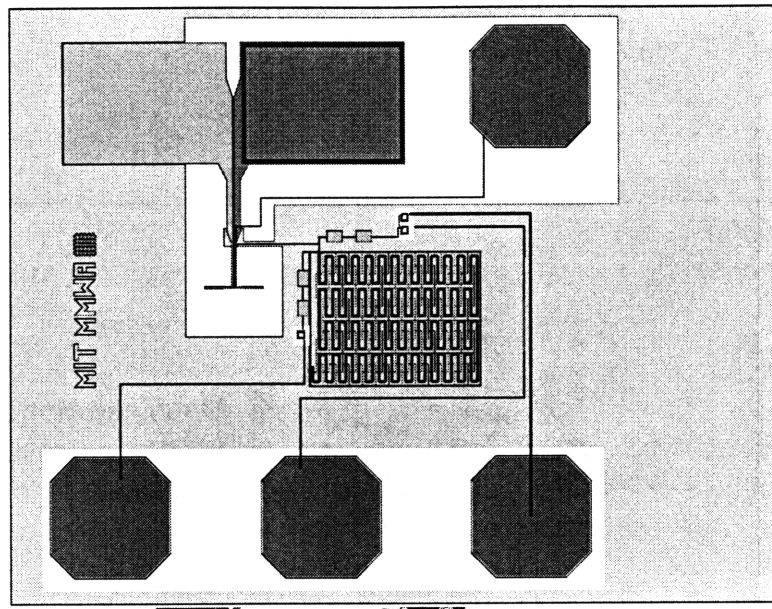


Figure 2-12: Planar picture of the receiver with the LO.

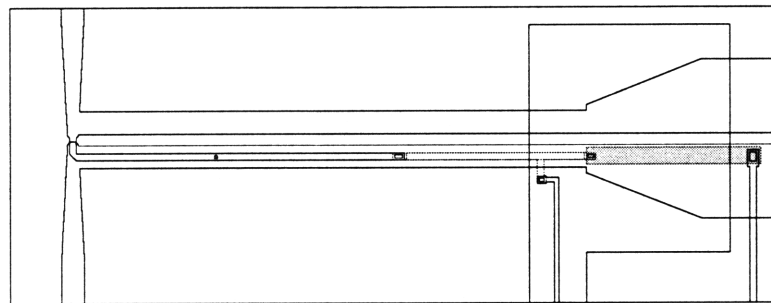


Figure 2-13: Detail of tuning and coupling structures.

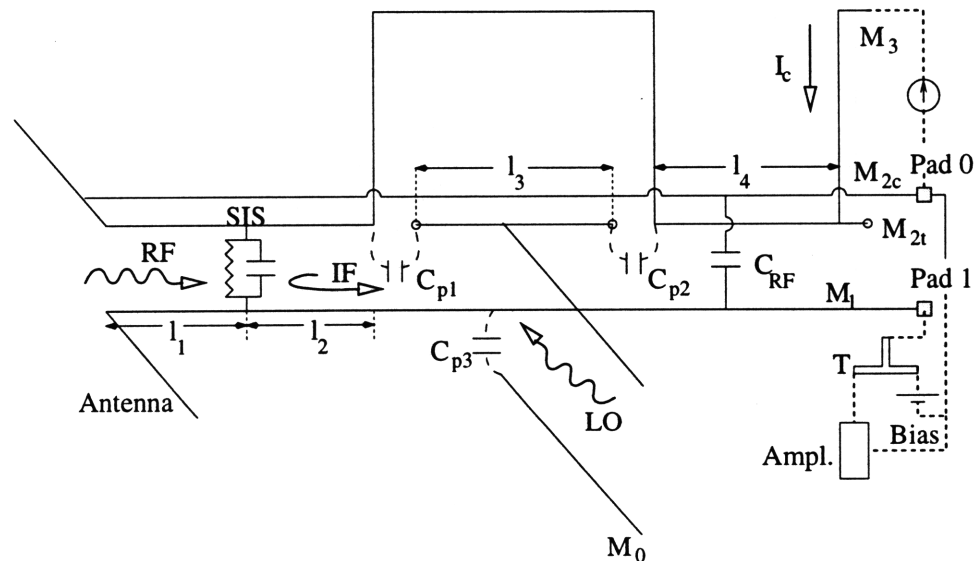


Figure 2-14: Circuit equivalent of the antenna with LO line and current control line.

calculation was made.

The LO signal is capacitively coupled to the  $M_1 - M_{2t}$ . The position where the interconnection is established is such that the resistance seen from that point is purely resistive. Again, detailed calculations taking into account T-microstrip structures and discontinuities were not done. So, it was assumed that the capacitors were shorted and the angles of the microstrips did not matter. For better coupling, other designs covered in most microwave textbooks can be tested in the future (e.g interdigitated coupler). The demand for resistive behavior was posed by Hypres Inc, because they had performed simulations with resistive loads. Non-resistive loads turned out to cause instabilities to the LO circuit.

## 2.2.5 Optics

For an imaging system, it is crucial to have the right spacing between the detectors. The dimensions of the machined apertures limit our flexibility for optimum separation, a simple calculation of which is given below.

We use the Gaussian optics formulation which facilitates the computations ([34], [35]). The power density of a Gaussian beam is given by

$$\frac{P(r)}{P(0)} = e^{-2(r/w(z))^2} \quad (2.12)$$

and the propagation of the waist obeys the equation

$$w(z) = w_0 \sqrt{1 + \left(\frac{z}{z_R}\right)^2} \quad (2.13)$$

where  $z$  is the direction of propagation,  $r$  is perpendicular to  $z$ ,  $w_0$  is the minimum beam waist and  $z_R = \frac{\pi w_0^2}{\lambda}$ ,  $\lambda$  is the wavelength. The  $\theta_{1/e^2}$  is derived by taking the limit of large  $z$  and small angle approximation ( $\tan(\theta_{1/e^2}) \approx \theta_{1/e^2}$ ), so  $\theta_{1/e^2} \approx \frac{\lambda}{\pi w_0}$  for  $r(z) = w(z)$ . The angle of half power  $\theta_{3db}$  is found for  $r(z) = 0.59w(z)$ , so  $\theta_{3db} \approx 0.59\theta_{1/e^2}$ .

When a thin lens is used and the incoming beam has its minimum beam waist  $w_0$  located at the focal distance of the lens  $f$ , the outgoing beam has minimum waist  $w_1 = \frac{\lambda f}{\pi w_0}$  located at the focal distance. Thus, we conclude from the above equations that  $\theta_{1/e^2} = \frac{w_0}{f}$  for the

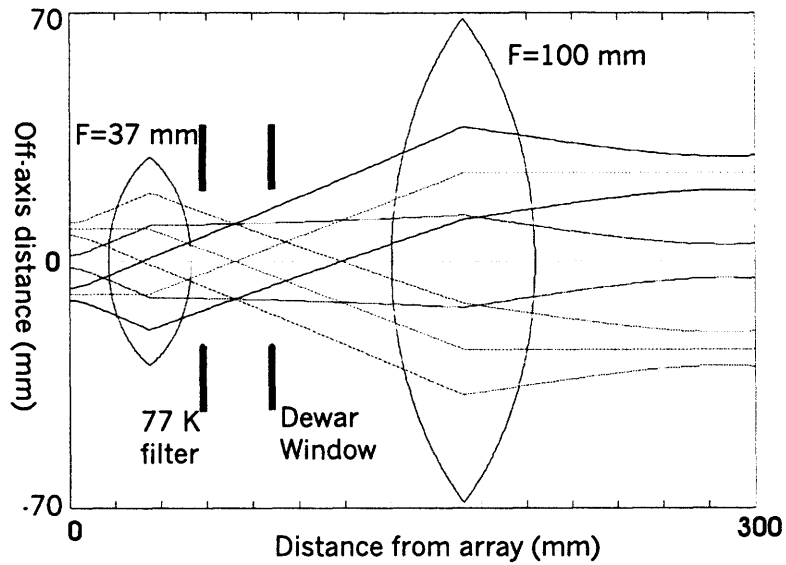


Figure 2-15: *Optical scheme of the imaging array.*

outgoing beam. For spatial separation  $d$  between two beams, the angular separation will be  $\theta_s \approx \frac{d}{f}$ . For imaging purposes, one of the requirements usually posed is  $\theta_s = 2\theta_{3db}$  which leads to the spacing rule  $d \approx 1.16w_0$ .

The size of the machined pyramidal horn is  $3.56\lambda$  which corresponds to  $5.6 \text{ mm}$  at 190 GHz. As a result of the split-block technique, the separation between the elements is  $6.5 \text{ mm}$ . The beam waist can be found to be  $w_0 \approx 1.75 \text{ mm}$  by noticing from simulated results that  $\theta_{1/e^2} = 16^\circ$ . Thus,  $d \approx 3.7w_0$  which implies an undersampling.

The optical system is a simple Gaussian telescope: it consists of two lenses separated by their respective focal distances. One of the features of this optical scheme is that the ratio of input and output waist is independent of the frequency of operation:  $\frac{w_{out}}{w_{in}} = \frac{f_2}{f_1}$ . The lenses, made of Teflon, have focal distances 37 mm and 100 mm, located inside and outside the cryogenic unit respectively. The choice of these focal distances is dictated by the limited space and the small window of the cryogenic unit.

A simulation using Gaussian optics is shown in Figure 2-15.

# Chapter 3

## Fabrication Steps and Preparation of the Experimental Set-Up

The implementation of the design discussed in the previous chapter depends highly on the quality of the fabrication steps and the preparation of the experimental set-up. This chapter focuses on the fabrication conducted at Lincoln Lab and at Hypres Inc. It was fortunate that our wafer supplier prepared high quality devices without noticeable deviations from our design. For the experimental set-up, there are many problems involved that one cannot easily resolve by searching the bibliography. Numerous "tricky" issues were solved by the the expertise of Gerhard de Lange.

### 3.1 Fabrication Steps

The imaging array of this project consists of the device wafer, the backing wafer and the aperture wafers. All must be micromachined to form the pyramidal cavity. The critical and still techologically challenging issue of SIS fabrication was conducted by Hypres Inc using the industrial design rules that have proven to be reliable over the time. Since we are dealing with many detectors on the same chip, uniformity and repeatability are very important in order to reach reliable conclusions about the future applications of the imaging array of this project. The micromachining of the device wafer took place at Hypres Inc whereas the micromachining of the rest of the wafers was completed by us at MIT Lincoln Laboratories.

A description of the current fabrication follows along with a brief mention of the fabrication of our former wafer supplier and members of this research group. We conclude this section by presenting the micromachining steps and the gold deposition process.

### 3.1.1 Device Wafer Fabrication

HYPRES Inc fabrication process makes use of niobium for the SIS junctions as well as for planar metallic circuitry. Niobium has a high critical temperature ( 9.5 K ), electrical and thermal stability and thermal cyclability. These characteristics make *Nb* the metal of choice. In order to solve the problem of oxidization, *Ti/Pb/Au* are used for the wafer contacts.

SIS junctions are formed by a trilayer deposited on the whole wafer to achieve uniformity. The wafers used are silicon wafers which are covered on both sides by low-stress silicon nitride of 1- $\mu\text{m}$  thickness fabricated by low-pressure chemical vapor deposition process (LPCVD). The trilayer consists of *Nb/Al-Al<sub>2</sub>O<sub>3</sub>/Nb*. The first *Nb* layer of the SIS junction is commonly called the base electrode and the second one the counterelectrode when viewed from the cross section. The SIS junction is defined by patterning the area of the counterelectrode. In this process, the capacitance of the junction is  $38\text{ fF}/\mu\text{m}^2$ .

The available layers for a typical fabrication process of HYPRES Inc when viewed from the substrate to the upper metallic contacts are the following:  $M_0$  *Nb* layer,  $I_0$  *SiO<sub>2</sub>* layer,  $M_1$  trilayer, *SiO<sub>2</sub>* layer,  $R_2$  resistive layer (1 Ohm/sq. ), *SiO<sub>2</sub>* layer,  $M_2$  *Nb* layer,  $I_2$  *SiO<sub>2</sub>* layer,  $M_3$  *Nb* layer and  $R_3$  *Ti* layer for contacts.  $R_2$  is made of *Mo*. The design rules for the various layers can be found in [36].

Since there are many layers available for the circuit designer, the fabrication steps are numerous.  $M_0$  *Nb* layer is deposited on top of the substrate and the area of interest is defined by spinning photoresist, developing, RIE etching of the unexposed  $M_0$  layer and stripping the photoresist (abbrev. PDRS).  $I_0$  area is formed by depositing *SiO<sub>2</sub>* and patterned by PDRS. Likewise, for the  $M_1$  trilayer. The trilayer is deposited in cryopumped load lock d.c magnetron sputtering system with a base pressure of better than  $5 \times 10^5$  Pa. All the metals (*Nb, Al*) involved in the trilayer are sputter-deposited in an argon plasma. After the first



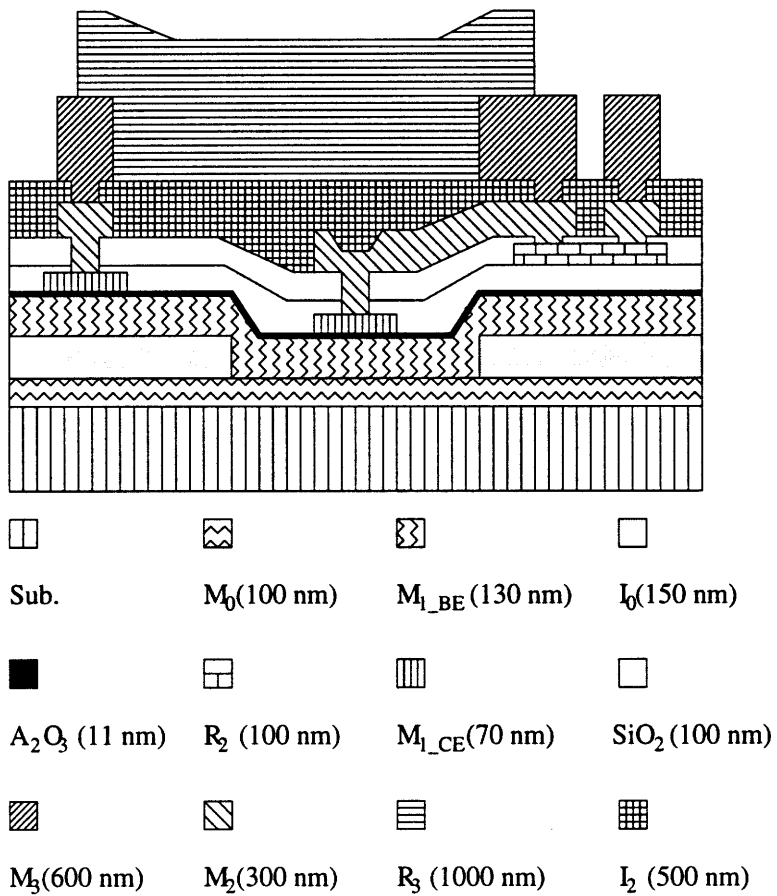


Figure 3-1: *Cross section of a typical Hypres wafer.*

layer of *Nb* and the subsequent layer of *Al*, follows the critical step of oxidation of *Al* to form the oxide of the SIS junction. The parameters that affect the current density of the junction are the oxidation time and the oxygen pressure. For a fixed oxygen pressure the current density decreases as a function of oxidation time and for fixed oxidation time the current density decreases as a function of oxygen pressure. As mentioned above, the SIS junction area is defined by the area of the counterelectrode. Thus, a photoresist layer is deposited and PDRS follows. After stripping the photoresist, a first layer of *SiO<sub>2</sub>* is deposited to serve as the substrate for *R<sub>2</sub>* resistive layer from which the resistor is defined by PDRS. On top, a second layer of *SiO<sub>2</sub>* is deposited. PDRS process results in the removal of the underlying *SiO<sub>2</sub>* in the regions of interest. *M<sub>3</sub>* layer is deposited on top and the designed planar circuit is formed by PDRS. Finally, Au contacts (*R<sub>3</sub>*) are made by spinning photoresist, developing, Au evaporation, and lift-off. A typical cross section of a processed wafer is shown in Figure 3-1.

The patterning of the SIS junction is still an important research issue in many research groups. Edward Garcia and Brian Jacobson in our group fabricated SIS junctions and antenna structures using SNAP (selective niobium anodization process ) [14]. The areas that are anodized are converted into niobium oxide of the counterelectrode layer. Thus, the required SIS space is protected during the anodization process. In the past, the supplier of device wafers was A. W. Lichtenberger's research group from the University of Virginia. Two approaches were adopted for the SIS definition [37]. In the first approach, SNEP (selective niobium etching process) was used and in the second, a modified SNEP was applied.

Hypres Inc makes use of a simple SNEP technology which is efficient for large SIS junctions. The counterelectrode is patterned with a mask and reactively etched by *CF<sub>4</sub>/O<sub>2</sub>* in a RIE system. The aluminum oxide acts as an etch stop and the junction is formed. A simplified flow process is illustrated in Figure 3-2.

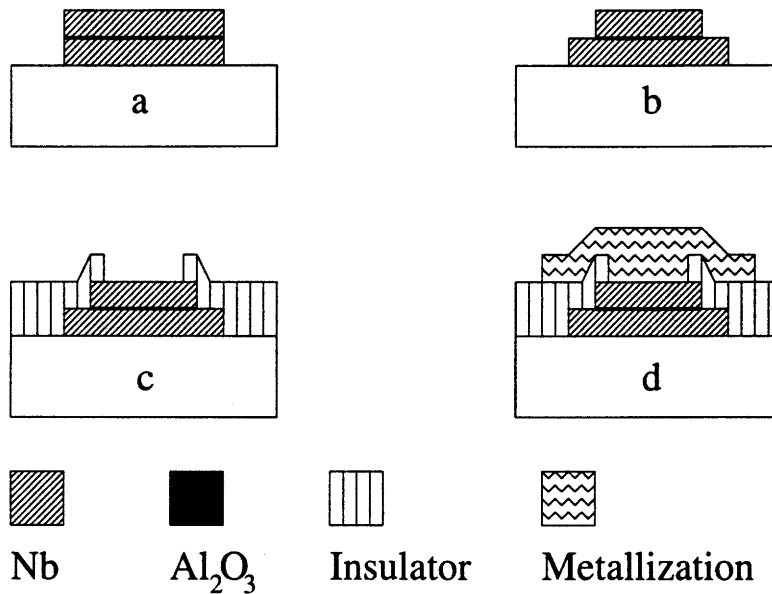


Figure 3-2: *Junction definition: (a) Trilayer deposition and base electrode definition; (b) junction definition; (c)  $\text{SiO}_2$  deposition and patterning; (d) wiring deposition and patterning.*

### 3.1.2 Micromachining Process

At Lincoln Lab, the *Si* wafers with the silicon nitride membrane on both sides are ultrasonically cleaned in acetone-methanol and rinsed in deionized water. In order to remove any organic residues, they have to be plasma-ashed for 2 min. Then, we spin positive photoresist AZ512, with a speed of 4000 rounds per min. It is a good practice before spinning to clean the wafer from any dust particles with nitrogen blow. In that way, the photoresist is uniformly distributed all over the wafer. The photoresist must be free from air bubbles which can cause nonuniformity. The photoresist is hardened by baking the wafer for 2 min at  $100^\circ\text{C}$ . The next step is the mask alignment. The appropriate mask, which is initially cleaned in nanostrip and rinsed in DI, is mounted over the *Si* wafer at the mask aligner. It is very important to align the crystal axis of the *Si* wafer with the mask. Any misalignment can cause shifted apertures during the step of anisotropic etching leading to a misaligned stack of wafers. The exposure time of UV radiation is 3.3 sec. Then, they must be developed (30 sec in 452 developer). The result of this step is the formation of exposed regions where the apertures will be created. The membrane is removed from these areas with RIE etching in a plasma of oxygen and freon for 12 min. The wafer is then cleaned

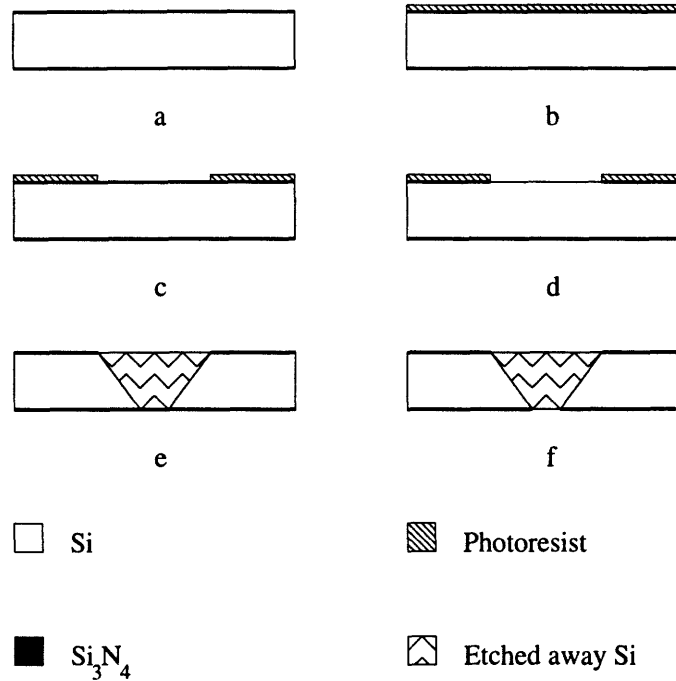


Figure 3-3: *Micromachining steps*

from photoresist and placed in KOH for anisotropic etching of *Si*. Brian Jacobson built a circuit for monitoring the level of water while the KOH is heated so that the required concentration is kept the same, which is 80% water and 20% KOH by weight [38]. Initially, it is heated for 4.5h at  $80^{\circ}\text{C}$  and then for 1h at  $60^{\circ}\text{C}$ . The result of this step is the formation of apertures in *Si* along the  $\langle 111 \rangle$  crystal axis. There is still membrane on the other side of the wafer which was not etched. It can be easily removed with a pointing q-tip. For any residues, the wafer is examined with a microscope. The various steps are shown in Figure 3-3.

The micromachining of the device wafer is not as straightforward as the previously described process. If the micromachining is conducted before the fabrication of the detectors, the device wafer must be handled with great care during the whole process due to the fragileness of the membrane [39]. If micromachining is the last step, the detectors must be protected from the KOH. Brian Jacobson performed micromachining at the end [38]. The device wafer is mounted in a specially designed teflon holder. KOH etching takes place on the exposed side of the device wafer while the other side is not facing KOH. This is achieved by the use of rubber o-rings between two teflon pieces and supply of nitrogen gas to assure

that the device wafer is firmly mounted minimizing the possibility of KOH leak. The RIE of the silicon nitride is done just before the micromachining. The drawback of this approach is the development of high temperature which may degrade the quality of the SIS junctions. In order to avoid that, long cooling between short periods of RIE is demanded as well as good thermal conductance between the wafer and the quartz plate of the etcher through which cool water flows. IR alignment is important before RIE in order to mark the areas of the dipoles where the free-standing membrane will appear. Gerhard de Lange performed RIE etching of the device wafers before the fabrication of the detectors. Alignment marks were necessary on the other side of the wafer for the orientation of the fabrication masks. Hypres Inc, our wafer supplier, also conducted micromachining at the end using a teflon mount. Another approach followed by [39], but for a different application, is to deposit silicon nitride on the side that must be protected and subsequently remove it.

### 3.1.3 Gold Deposition

The lossy sidewalls of the *Si* cavity formed by the individual wafers must be coated with gold since the theory developed for these receivers assumes conductive sidewalls. This step takes place at Lincoln Lab (group 86). Prior to the gold deposition, *Ti* is used (200 Å) as a first layer. In that way, *Au* can easily stick to the surface. A typical thickness is 4000 Å. Gold is evaporated through a shadow mask which was made at Lincoln Lab by laser cutting technique. Since the wafers must be mounted on a metallic surface which fits in the evaporator, it is very dangerous to break the fragile membranes of the device wafer. Thus, we use a dummy *Si* wafer where we spin FCS photoresist. During the baking process we stick the device wafer on top with the membranes touching the *Si* wafer. In that way, the membranes are protected from the rough metallic mounting surface. For the aperture wafers, the above step is not necessary. The shadow mask is aligned by eyeball and then a microscope is used for finer alignment. The result is satisfactory and the diffraction effects are negligible.

## 3.2 Preparation of the Experimental Set-Up

After the device wafer and the aperture wafers have been fabricated, the mounting process follows resulting in a stack of wafers. This stack must be aligned to the machined section, the magnet, the DC-IF board and then placed in the dewar where all the necessary connections must be completed. The cryogenic unit and its efficient operation are fundamental for the measuring process. All the above issues are discussed and we conclude with the description of a biasing circuit assembled at MIT for the array of detectors.

### 3.2.1 Mounting Process of the Wafers

An essential part of the mounting process is a  $x$ - $y$ - $\theta$  stage designed by Gerhard de Lange. By adjusting three different screws, a circular disk of the stage can move in an orthogonal fashion ( $x$ - $y$  correction) as well as in a circular fashion ( $\theta$  correction). A microscope slide is glued on the disk with superglue (krazy glue). The building of the stack follows the order: first backing wafer, second backing wafer, device wafer, last aperture wafer. The  $x$ - $y$ - $\theta$  stage is placed on a hot plate at approximately  $150^{\circ} C$ . Then, the first backing wafer is placed on the glued slide with the opening cavity angle facing up. Small amount of bee wax is cut. When the stage is hot enough, we place the bee wax pieces with a razor near the four corners of the wafer so that the wax will penetrate below the wafer. For uniformity of bee wax, we may use a pair of q-tips to press the two opposite corners of the wafer. In that way, the little bee wax bumps are avoided. The stage is then removed from the hot plate using a pair of tweezers. Sometimes during this process, bee wax can stay on top of the wafer. In that case, it must be carefully removed with a q-tip immersed in hot TCE.

The second wafer is placed on top of another microscope slide that is heated on the hot plate and the same process of gluing with bee wax is repeated. This wafer must have the the opening cavity angle facing the slide. By eyeball, a first alignment is done after sliding the second wafer over the first wafer (the wafers touch each other). For better alignment, a microscope must be used. The alignment is facilitated by simultaneously examining many antennas. Having achieved a first rough alignment of the backing cavity to the second wafer, we must use the jug that holds the machined section of the array. This jug fits exactly

the  $x$ - $y$ - $\theta$  stage with properly placed dowel pins. We put a small quantity of superglue on the two sides of the jug, place it carefully on the stage and press it. In that way the microscope slide with the second wafer is glued on the jug. Having now the jug on top of the stage, we can move it for precise alignment. First, the angle  $\theta$  is adjusted in such a way that all the backing cavities have the same  $x$  and  $y$  margin from the apertures of the second wafer. Second, the  $x$  and  $y$  adjustment is performed. We can do that by concentrating on one element since all the elements of the array will be aligned at the same time.

After we are certain that the alignment is satisfactory, the jug is removed and we put a small quantity of superglue at the corners and the midpoints of the wafer. Then, we press the jug against the stage and keep it firm for a minute. In the meanwhile, it is a good practice to look at the profile of the first stack to inspect any possible airgaps. If they exist, we press also the slide at the points of airgaps. That's why it is important to have uniformity of bee wax. The amount of superglue must not be excessive because it will spread all over the cavities. I found this step of alignment not very easy since the area of the first cavity is very small. The dowel pins have some degrees of freedom so a relative  $x$ - $y$  movement is possible that may destroy the alignment. An approach I was usually following was to press the jug in one direction,  $x$  or  $y$ . During the gluing process, I kept pressing in the same direction. Unfortunately, it didn't work all the times and misalignments could not be corrected because the wafers were firmly glued together. For extreme misalignments, the first stack must be immersed in acetone and dissolved. Sometimes, this can take a few hours and other times a couple of days.

Having glued the two wafers, the  $x$ - $y$ - $\theta$  stage along with the jug is placed on the hot plate. When the temperature is high enough, we carefully remove the jug. Two things may happen: the stack remains on either the stage or the jug. In either case, we put it again on the hot plate and when it is hot enough, we slide the stack with a  $q$ -tip away from the microscope slide. It is important to keep in mind that superglue cannot withstand high temperature for a long time and it starts melting. This problem occurred many times in the past and the alignment of the wafers had to be redone. If the procedure is successful, we immerse the stack in hot TCE ( $100^{\circ} C$ ) for 5-10 sec to remove the bee wax.

The same procedure is followed for the rest of the wafers. In that way, the whole stack

is formed. When we place the device wafer, careful gluing is needed. In case the device wafer is not glued well on top of the stack of the backing wafers, pulling the jug out may destroy many membranes which were glued. So, we must make sure that the stack is firm and the wax has completely melted. Extra care of the device wafer is needed also during the  $x-y-\theta$  alignment because the fragile membranes touch directly the stack of wafers. A good habit is to lift the jug slightly during the alignment process avoiding any friction on the membranes.

Once the stack of wafers is formed, it must be aligned with the machined section. The same process is followed with the only difference that the machined section is now screwed on the window of the jug and when we place the stage and the jug on the hot plate, the stack is detached from the jug where the bee wax exists.

It is essential to have a firm stack because during the four times that we use the hot plate a weak superglue layer between two wafers may loosen up.

### **3.2.2 Preparation of the Experimental Set-Up on the Cold Plate of the Dewar**

The stack of wafers is formed in such a way that the antenna pads are now exposed via apertures of the first backing wafer. Access to these pads is achieved with miniature bellows. During the whole process we may touch the antenna pads, so it is advised to wear an electrostatic discharge wrist to avoid destroying SIS junctions. The miniature bellows are placed in the apertures of the pads in such a way that the holes of the bellows are facing upwards. Then, the magnet is mounted. Holes in the magnet have been drilled so that the DC-IF board can have access to the bellows. This is done using microscrews and coaxial cables for the two antenna pads. The microscrews are screwed in the copper body of the magnet which is grounded while the coaxial cables stay firm with crystal bond. For the 9 antennas we have 18 pads. It is desirable to establish contact between the microscrews and all the antennas. Since the miniature bellows are not fixed in the apertures, it is not easy to have contact with all the antennas. The only possible view for finer orientation of the magnet is the side view which gives a 2D picture of the microscrews. Trying to access



many antenna pads, I destroyed a number of miniature bellows. Given the high cost of the bellows, it is preferred to have a moderate number of antennas with easy access. A better choice will be the permanent fixing of the bellows on the microscrews of the magnet. But even in this case, extra care is needed because excessive pressure on the miniature bellows can destroy their elasticity which is very important, especially when they are operated at low temperatures.

Gerhard de Lange had experimented for a long time with a number of contacts. Pins glued with silver epoxy was one of them. The pins alone were not an ideal solution because a good contact at room temperature was not preserved at 4.2 K. Apparently, the pins lose their elasticity. Then, epoxy was used at the apertures of the pads. Although the contact was better in this case, the wafer could not be easily reused because of the properties of epoxy. For its removal, Ecostrip is used. Unfortunately, the dissolved epoxy spreads all over the wafer shorting conductive areas. In addition, epoxy may press the wafers in such a way that cracks can occur. The idea of miniature bellows that Gert de Lange came up with was a clean and reliable solution.

The magnet fits to another copper frame which is screwed on the jug. In the past, it was noted that excessive pressure of the stack of wafers can result in cracking the stack. For this reason, a protective U-shaped copper frame is placed between the machined section and the magnet. Thus, the pressure is exerted on the machined section and the stack of wafers suffers only from the pressure of the microscrews of the magnet whose lengths can be adjusted. Sometimes, it was necessary to screw them further for better contact while the magnet frame was firm.

On top, the DC-IF board is mounted. It is essential that the microscrews are clean from crystal bond so that the electrical contact is established. The DC-IF board has proper connections for the IF signal and the bias of the SIS devices. On one of the corners of the jug, the temperature sensor is placed giving a representative temperature of the actual SIS device. For good thermal contact, indium foils are stacked between the temperature sensor and the jug. In addition, indium foils are used also at the bottom of the jug that touches the cold plate of the dewar. A metallic strip connecting the jug to the cold plate is also used for better thermal contact. Here, it is worth noting that the actual temperature of the junction

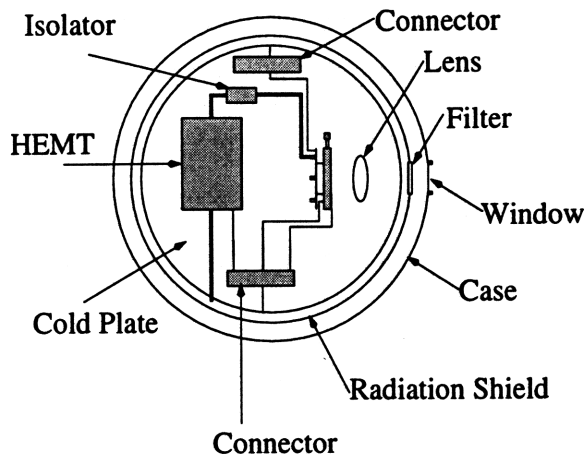


Figure 3-4: *Top schematic of the cold plate.*

is higher since the membrane is not a good thermal conductor. As there is a significant amount of metal touching the cold plate, it is imperative to have optimum thermal coupling. Otherwise, the process of cooling down the cryogenic unit can be lengthy and the hold time at 4.2 K be short. A coaxial cable connects the IF output of the DC-IF board with an isolator placed on top of the cold plate. The isolator is connected to the IF amplifier of the cryogenic unit. Only one IF signal can be connected to the IF amplifier. The amplified IF signal is brought outside the cryogenic unit. The magnet wires, the temperature sensor leads and the bias wires are directed to connectors with permanent output wires going outside the cryogenic unit. The cryogenic rules for connecting 4.2 K parts with 300 K parts call for wires made of Constantan or Manganin of small diameter. In that way, their highly resistive nature guarantees poor thermal conductance. In front of the machined section, a permanent teflon lens is placed. A simplified schematic is shown in Figure 3-4.

### 3.2.3 Description of the Cryogenic Unit

The cryogenic unit consists of a nitrogen and a helium tank (Figure 3-5). A radiation shield surrounding the helium tank is connected to the 77 K tank. In that way, the dewar can stay for a longer time at 4.2 K. The set-up rests on the cold plate of the helium tank. Since external radiation must be coupled to the detectors, a hole in the radiation shield and the case is opened. The manufacturer advises minimum number of holes for long lasting low temperature. In order to avoid excessive heat of the 300 K blackbody, a PTFE

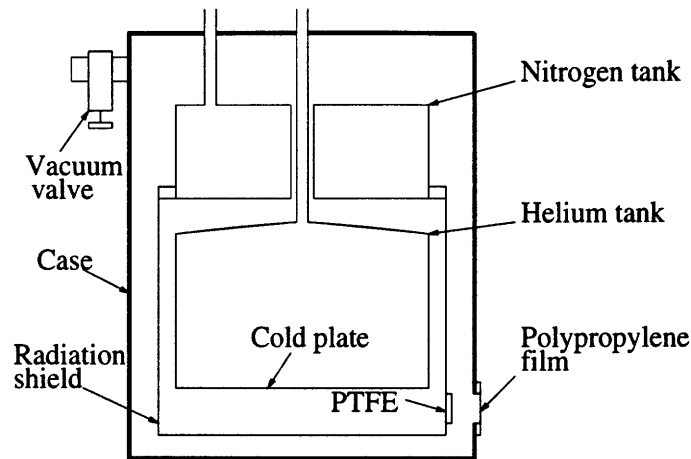


Figure 3-5: *Cryogenic Unit.*

(PolyTetraFluorEthylene) disk is placed in the hole. This 77 K filter has the property to be almost opaque to visible and infrared radiation and transparent to millimeter waves that we test ([40]). Thus, we achieve less consumption of He. The space left on the cold plate for the experimental set-up is limited. This fact does not allow flexibility for the we use. Part of the external radiation of the Gunn oscillator is lost because of the dimensions of the window. The window consists of two metallic rings mounted on the case and a 1.2 mil polypropylene film placed in between with vacuum grease. For low noise level, thin films of low absorption are required. The disadvantage of using thin films is their inherent low strength. After a couple of uses, I noticed that the cooling was not satisfactory due to vacuum leaks. The film is deformed because of the significant pressure difference between the atmosphere and the interior of the dewar. So, frequent changes of the film were necessary. Thicker films are obviously more robust but add more noise. The absorption of the polypropylene film we used is about 98-99 %. The air that surrounds the tanks is pumped via a vacuum valve connected to the dewar's case. More details about the cryogenic unit can be found in [41].

### 3.2.4 Biasing Circuitry

For real applications involving the array of detectors, the SIS devices must be independently biased at their optimum (I,V). In addition, all the different IF channels must be available for simultaneous processing to justify the characterization imaging array. The former was accomplished by building a biasing box for all 9 SIS junctions. The latter remains to be



A particular feature of the design is the different modes of operation: V-mode and I-mode. In the first case, the circuit operates as an ideal voltage source and in the second case as an ideal current source. Thus, for an I-V curve, the load line is perpendicular in V-mode ( $R_{int} = 0$ ) and horizontal in I-mode ( $R_{int} = \infty$ ). For video and heterodyne detection, it is very important to refer always to a constant voltage point in order to measure  $\Delta I$  for the former and  $\Delta P_{IF}$  for the latter. The operation of an ideal voltage (current) source is achieved by feedback techniques: when the voltage (current) increases for a constant bias point, a negative feedback is directed to a voltage (current) driver and the operation is stabilized.

Additional features are: variable frequency of the voltage or current sweeper to have the flexibility to use an oscilloscope (fast sweeping) or a plotter (slow sweeping), variable voltage and current range/gain, external input for computer-controlled sweeping, variable low-pass filters to reduce noise signals.

The initial design was for a single SIS junction. This design was repeated 9 times to complete the biasing box. The circuit was printed at Lincoln Laboratories on 3 PC boards, each hosting 3 units. Some operations are global in the design so interconnections had to be done. Unfortunately, the interconnections were numerous and the number of wires not easily manageable. In addition, the accessibility of components became difficult due to the wires. Although the assembly was accomplished, it is advised for future attempts of the reader of this thesis to use printed paths and limited, if not at all, number of wires. Printed paths minimize also the voltage drops which occur at the usual wire connections. Another annoying problem that emerged during the testing process was that many TTL switches were quasi-operating. This was due to the fact that the potential drop after some units was so significant that the voltage level could not be recognized as a logic 1 or 0 leading to unpredictable results. A very handy solution was the use of a follower.

The full design can be found in the Appendix.



# Chapter 4

## Measurements

This chapter focuses on the measurements conducted during the project. Video detection is used for beam pattern and fourier transform spectroscopy measurements, and heterodyne detection for noise temperature measurements. Furthermore, the quality of SIS junctions is examined from their DC operation and the operation of Josephson junction local oscillator is investigated from some first rough data. We will try to show that uniformity of operation across the array elements has been satisfactorily achieved and low-noise performance has been reported ([42]).

### 4.1 Array Unpumped I-V Characteristics

The uniformity of the unpumped I-V characteristics of the imaging array was examined, at a bath temperature of about 2.7 K. The measurements were not conducted in one step due to the difficult alignment of the miniature bellows connecting the antenna pads to the DC-IF board. While the set-up was prepared for heterodyne measurements of a single detector, the unpumped I-V characteristic was the last step to characterize the SIS junction itself. Thus, the solid-state device is separated from its electromagnetic environment and the quality of fabrication is examined.

For  $J_c = 5 \text{ kA/cm}^2$  and area of junction  $3\mu\text{m} \times 3\mu\text{m}$ , the theoretical value of the normal resistance is  $5 \Omega$  for gap voltage  $2.9 \text{ mV}$  of *Nb*. The measured gap voltage for the devices across the array was in the range of  $2.4 - 2.5 \text{ mV}$  while the resistance was in the range

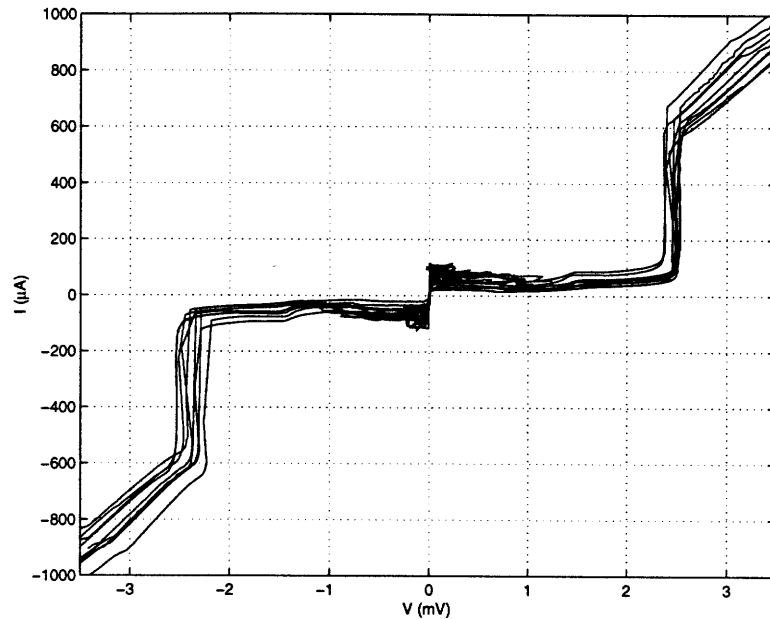


Figure 4-1: *Unpumped I-V characteristics across the imaging array.*

3.5 - 4.5  $\Omega$ . The leakage current is below 120  $\mu A$ . For high voltages the current starts to bend downwards. Another interesting observation is the back bending of the current rise at the gap voltage. The I-V curves are shown in Figure 4-1.

The lower value of resistance can be due to a larger area of the SIS junction or an increased critical current density. The back bending is an indication of higher local temperature. From BCS theory, the gap voltage decreases with increasing temperature. As the current rises, the local temperature gradually increases leading to the back bending. This feature of the I-V characteristic is also due to the poor thermal conductance of the membrane. The increased local temperature can also explain the bending of current for high voltages. As the current increases above the gap voltage, the temperature increases leading to a higher resistance.

As a general conclusion, we could claim uniformity across the elements of the array in their DC operation and high quality fabrication procedure as the sharp current rise indicates.

## 4.2 Noise Measurements



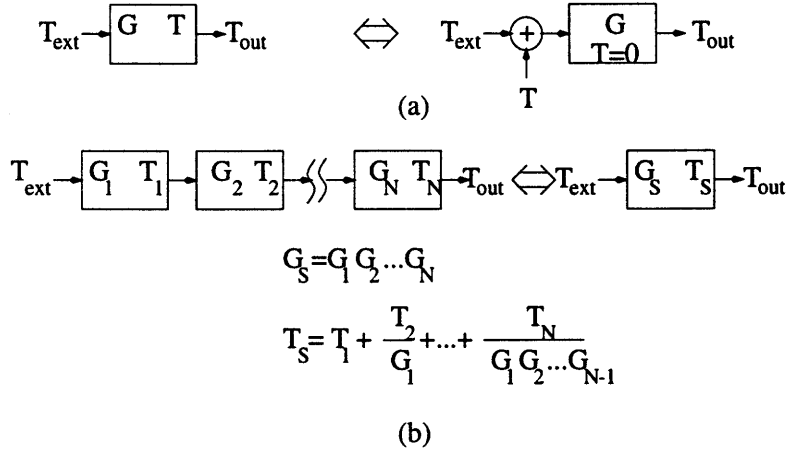


Figure 4-2: (a) Definition of noise temperature, (b) noise temperature chain rule.

In radio astronomy where SIS junctions are mainly used, the scientific community talks in terms of temperature to indicate power level. To convert to power, we apply Rayleigh-Jeans limit of Planck's law:

$$P_s = k_B T_{eq} B \quad (4.1)$$

where  $B$  is the bandwidth of interest,  $k_B$  Boltzman's constant. When a system of gain  $G$  is not noise-free, it is characterized by its noise temperature  $T_N$ . This is defined as the temperature (that is, power) that we have to feed an equivalent noise-free system to get the same output noise temperature (Figure 4-2, (a)). For a cascade of 'noisy' systems, the equivalent noise temperature can be found by applying the rule of Figure 4-2 (b). This chain rule suggests that the first stages must be as less noisy as possible for low equivalent noise temperature of the compound system. If a system is characterized by attenuation, that is gain less than unity (e.g beamsplitter), the equivalent noise temperature is given by

$$T_s = T_{amb} \frac{1 - G}{G} \quad (4.2)$$

where  $T_{amb}$  is the ambient temperature and  $G < 1$ . A figure of merit widely used instead of the noise temperature is the Y-factor, commonly referred to 77 K and 300 K load,

$$Y \equiv \frac{P_{out}(300, f)}{P_{out}(77, f)} \quad (4.3)$$

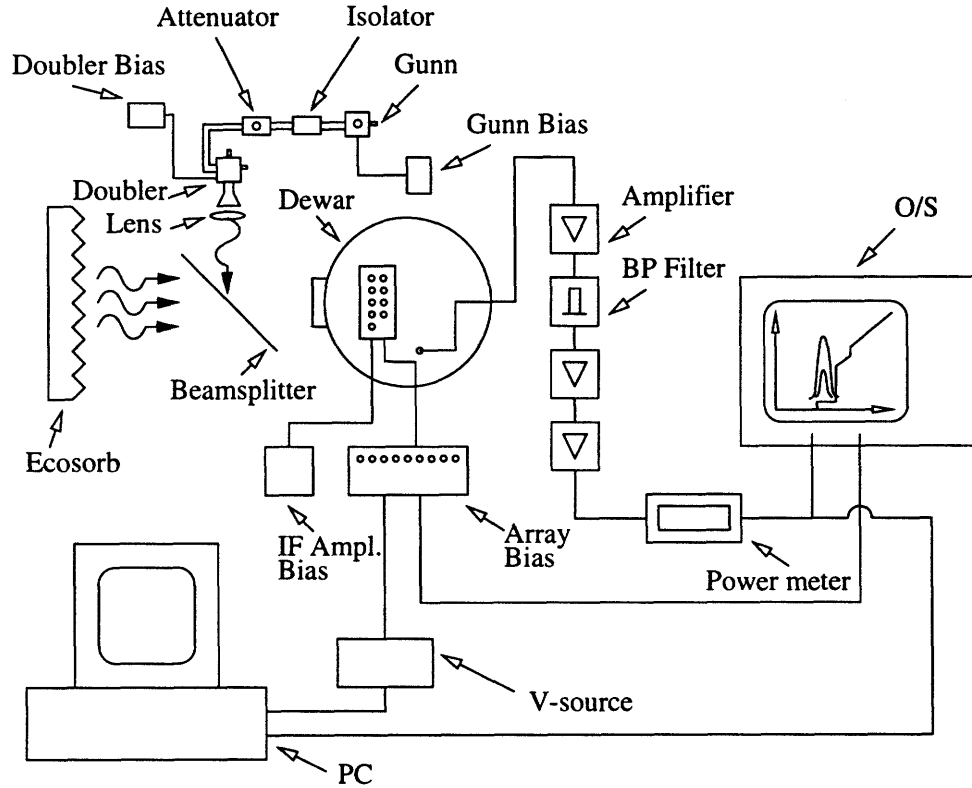


Figure 4-3: *Experimental set-up for heterodyne measurements.*

where  $P_{out}(T, f) = G(P_{in}(T, f) + P_N)$  and  $P_N = k_B T_N B$ . The idea behind this figure of merit is to be able to extract the noise temperature of the system without knowing  $G$ , by applying two calibrated input power levels,  $P_{in}(300, f) = 300k_B B$ ,  $P_{in}(77, f) = 77k_B B$ . Thus, if we solve for the noise temperature of the system, we end up with

$$T_N = \frac{300 - 77Y}{Y - 1}. \quad (4.4)$$

If we take into account the weak power level of the signals used in radio astronomy, a sensitive receiver is characterized by its low noise temperature for the frequency of interest. The experimental procedure is quite simple in principle: the IF power is measured at the first photon step for two black body loads (300 K and 77 K). The Y-factor is extracted yielding the equivalent noise temperature of the system.

#### 4.2.1 Experimental Set-Up and Measurements

Figure 4-3 illustrates the experimental set-up for hot-cold load measurements. The signal of the local oscillator is generated by a Gunn oscillator operating in the region of 95 GHz. The signal is guided to a doubler via an isolator and an attenuator. The isolator prevents the signal from being reflected back to the source and the attenuator regulates the power level that is desired for the output signal. The generated signal is in the region of 190 GHz. Backshorts located at the Gunn oscillator and the doubler provide fine tuning of the power level. A Teflon lens in front of the doubler provides better focusing of the outgoing beam. A beamsplitter made of polypropylene reflects about 2-3% of the LO signal to the dewar's window. A piece of Ecosorb in front of the beamsplitter serves the role of the calibrated input signal of a black body. When immersed in liquid nitrogen, we have the cold load of 77 K, and 300 K otherwise. The generated IF signal after the preamplification inside the dewar is externally amplified by a series of 3 amplifiers with total gain approximately 75 db. A bandpass filter centered at 1.5 GHz with 35 MHz bandwidth filters the signal from noise outside the frequency window of interest. A power meter indicates the power level of the amplified and filtered signal. The power level is displayed in the oscilloscope and feeds the PC. If the amplified power level saturates the power meter, an attenuator of 10 db or 20 db is placed in between.

Having fixed the frequency of the Gunn oscillator by turning a Vernier knob, the beamsplitter is replaced by a metallic surface. We want initially to see if radiation can be coupled to the detector. In order to achieve this, the mirror must have the proper angle especially when the off-axis elements are tested. Sometimes, the dewar had to be tilted and the lens in front of the doubler had to be adjusted. We have a good coupling when we manage to saturate the device, that is, the SIS junction behaves like a resistor with no gap. The backshorts of the LO chain are adjusted for stronger saturation. The mirror is subsequently replaced by the beamsplitter at exactly the same position. This cannot be achieved in practice but at least we have a first estimate of the way we should tilt the beamsplitter and we know that the power level is optimum. Another complication arises from the fact that only 2-3% of the signal is reflected by the beamsplitter. Many times I faced the problem of coupling LO signal since it was so weak that no photon step was observed. If this happens, one cannot actually know whether it is the power level or a misalignment of the optics chain.

Applying a trial-and-error procedure, the optics are optimized and if necessary, a thicker beamsplitter is used. In general, we don't want a thick beamsplitter because it introduces more noise to the system as explained earlier, but if no photon step is observed, that is the only way to perform heterodyne mixing. The SIS junction is biased in the region of the first photon step and the biasing box operates at constant voltage (V-mode). The power level is tuned with the attenuator and the backshorts to get the maximum IF power level. The bias point is set at the point of maximum power. It is crucial to have a photon step which does not suffer from the Josephson effect. When Josephson currents are present, the current does not stay fixed in time and the noise temperature results are deteriorated. The Josephson effect can be significantly suppressed by applying a current to the magnet. A current of about 0.1 mA is sufficient. Excessive supply of current will raise the temperature leading to He boiling. It is not necessary to keep the current source connected all the time. If the I-V curve looks satisfactory, the current can be gently decreased. Another way to insert magnetic flux to the SIS junctions is to change the mode of the biasing box, from V-mode to I-mode and back to V-mode. Similar results can be achieved by switching on and off the bias of the cryogenic preamplifier. The power meter is set in db scale. Placing the hot and cold load results in the Y-factor. The Y-factor is then converted to noise temperature. Different frequencies are tested and the center frequency of the BP filter is optimized for best noise temperature results. For complete I-V characteristics, the voltage sweeping is conducted externally by the computer which controls the voltage source of the lock-in amplifier.

The  $I - V$  and  $P_{IF} - V$  characteristics across the elements of the array are shown in Figure 4-4 for the  $140 \mu m - 190 \mu m$  design. LO power was coupled to the detectors #4, #5, #6 with a thin beamsplitter and for the rest a thick beamsplitter was used. Thus, the results that are presented are not strictly comparable but they give a good indication of the general trend. As expected, the center element outperformed the rest by achieving the lowest noise temperature of 62 K. The optics for this detector are less critical and sufficient LO power and hot-cold radiation can be coupled. The other elements in the same horizontal row (#4 and #6) didn't have difficulty in power coupling. For the rest, the hot-cold load measurement was time consuming and in general difficult. The cold load had to be rotated in a certain angle to get the real Y-factor. At the same time, it should not be near the

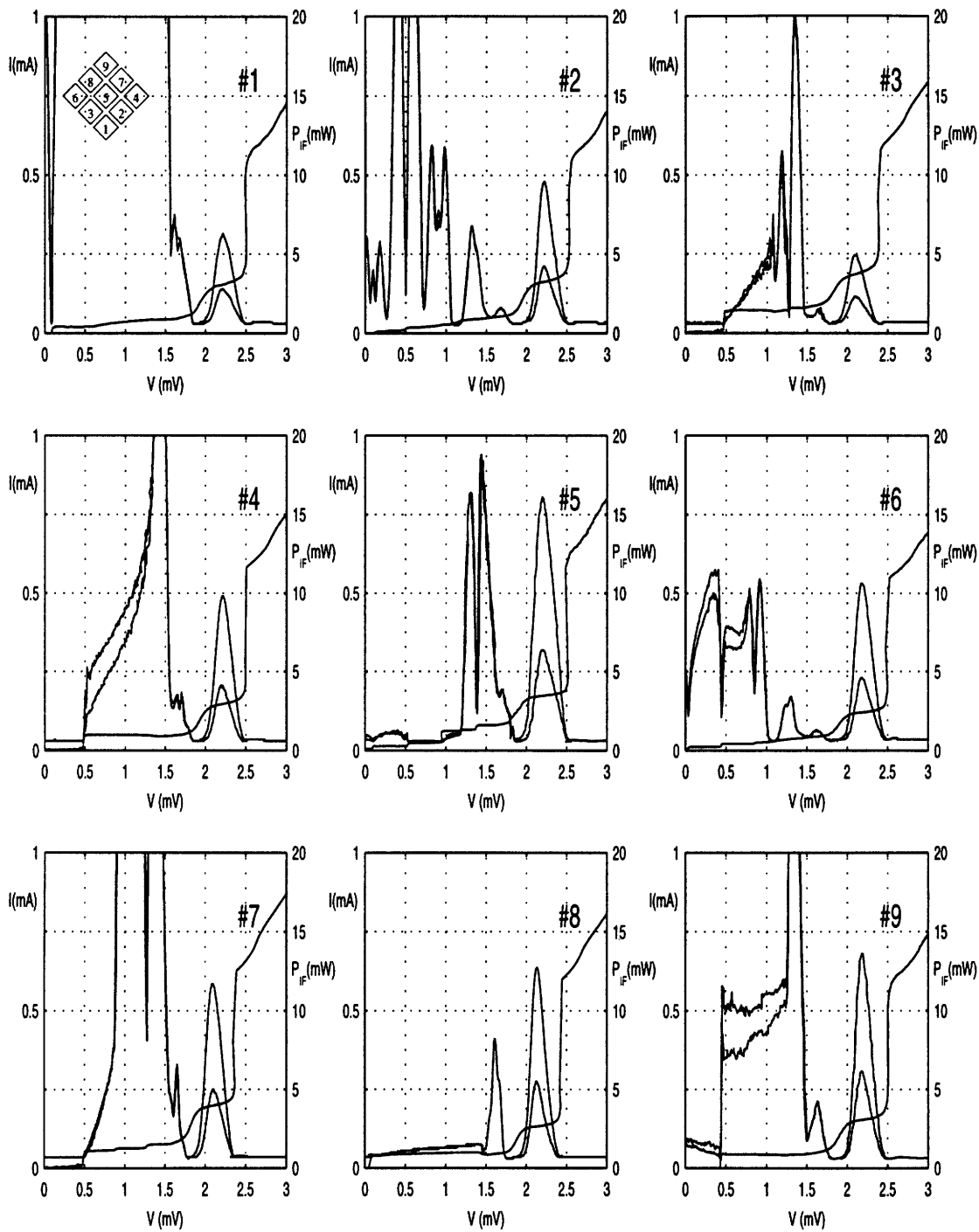


Figure 4-4:  $I$ - $V$  pumped characteristics and  $P_{IF}$ - $V$  for hot-cold load across the array.

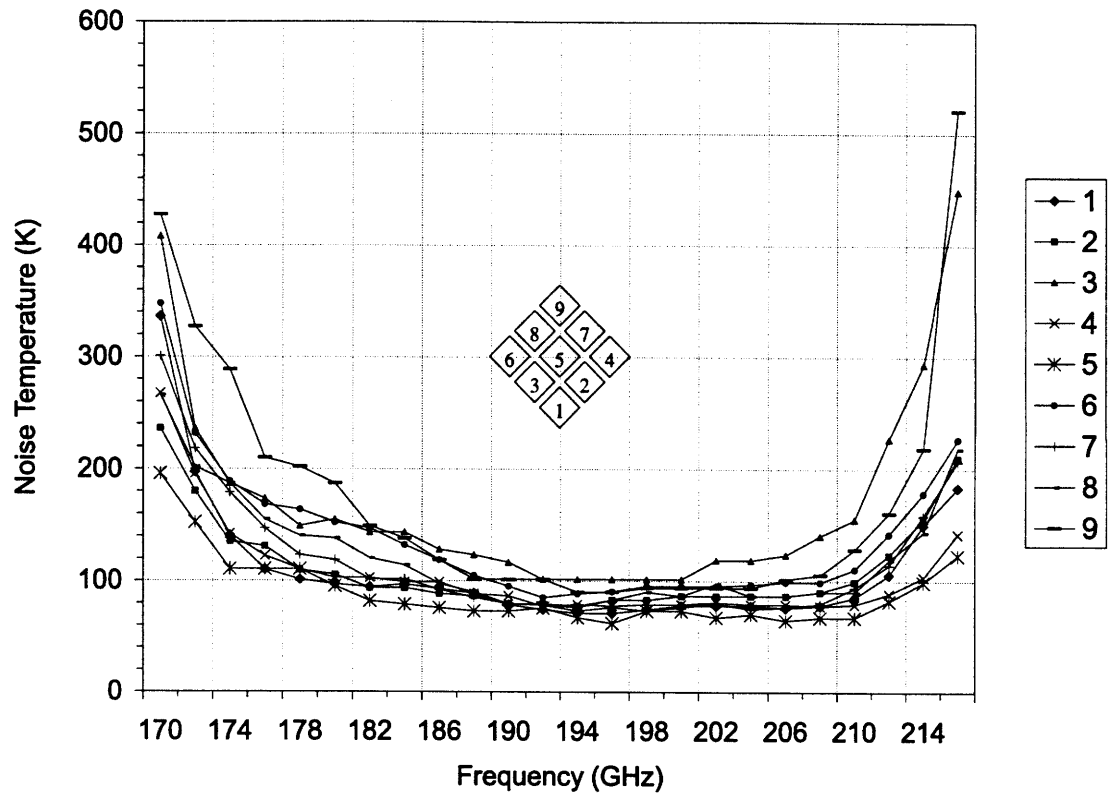


Figure 4-5: *Noise temperature vs frequency across the array.*

beamsplitter because the metallic surfaces of the beamsplitter contribute as an additional load. For computer measurements, the cold load was held in front of the detector only when the voltage was in the range of the first photon step. That was to ensure that the temperature was very close to 77 K. A non-scientific but rather useful advice: handle the cold load carefully, nitrogen leaks can cause severe burnings.

In order to discuss about comparable magnitudes, we must have the same system which means a common beamsplitter. By measuring the Y-factor of the same set-up but with two different beamsplitters, the cold load of 77 K had to be interpreted as a 84 K load. In that way, the system is characterized by excluding the effect of the beamsplitter. Doing this legitimate conversion, the noise temperature across the array in the frequency domain is presented in Figure 4-5. The lowest noise temperatures are in the range of 62 K-102 K. The elements across the array show a considerable uniformity. The bandwidth is about 40 GHz. When Gerhard de Lange conducted a similar experiment with a different wafer, he

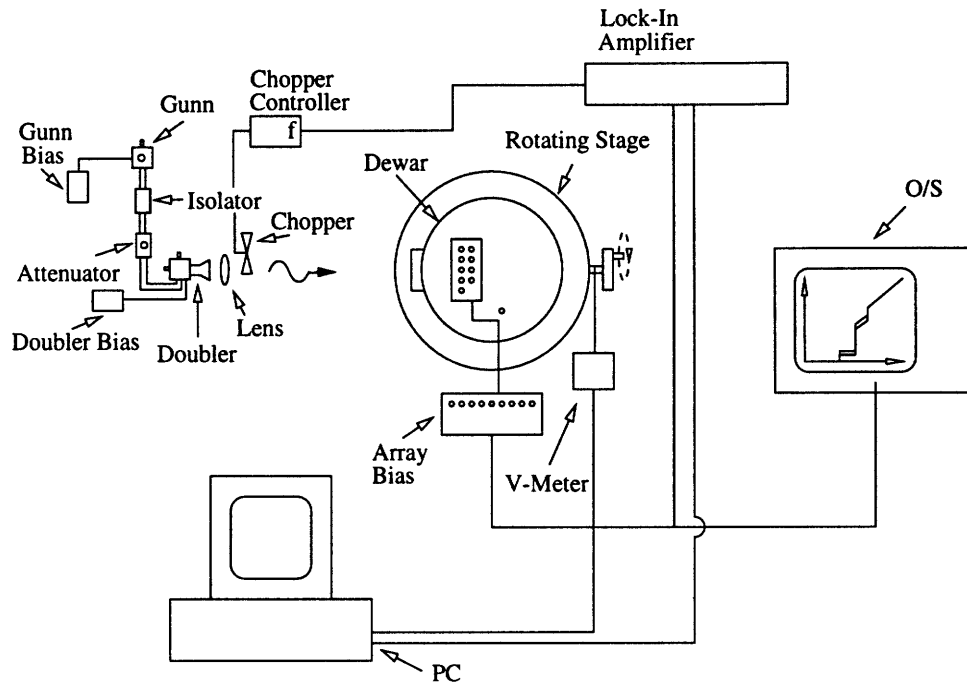


Figure 4-6: *Experimental set-up for beam pattern measurements.*

achieved a noise temperature of 52 K. These results are undoubtedly very optimistic and rank our detectors among the best reported so far in this frequency region ([22],[23],[24]). The best noise temperature is 45 K ([22]). If a better optical scheme is used, the noise temperature can be further reduced.

### 4.3 Beam Pattern Measurements

For beam pattern measurements, direct (video) detection measurements are conducted. As we discussed in earlier chapter, SIS devices can reach the quantum limit where the responsivity is constant. Thus,  $\Delta P_{RF} \propto \Delta I_{dc}$ . The power that is coupled to the device can be directly associated with the current changes which can be easily traced.

#### 4.3.1 Experimental Set-Up and Measurements

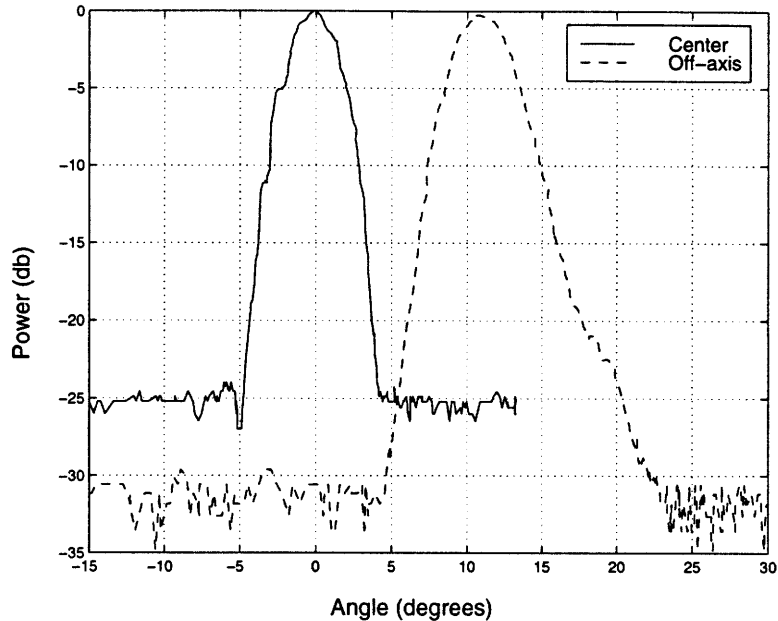


Figure 4-7: *Beam pattern measurements of elements #5 (center) and #4 (off-axis).*

The LO chain is fixed and the dewar is manually rotated. This is unavoidable because the LO chain is very fragile and any movement could be catastrophic, especially for the sensitive doubler. It is not feasible to detect changes of current in the GHz region. Thus, a chopper is used in front of the Teflon lens to form 'power packets' in the Hz region. These low-frequency changes can be detected by a lock-in amplifier. The SIS is biased at the first photon step (V-mode of the biasing box). The current signal is driven to the lock-in amplifier which is also fed by a signal of the chopper. Since both signals are of the same frequency, locking is achieved. The differential current level is a direct indication of the RF power level. It is not necessary to illuminate the detectors with excessive RF power because it can easily saturate the device. In addition, the responsivity reaches the quantum limit for weak signals. Thus, an attenuator is very useful. A voltage level proportional to the angle and the differential current feed the PC. It is unfortunate that the antennas are not optimally oriented but are tilted by  $45^{\circ}$  on this measured plane.

Beam pattern measurements of the center (#5) and off-axis element (#4) are shown in Figure 4-7. The 10 db beamwidth is  $5.8^{\circ}$  for the center element and  $7.6^{\circ}$  for the off-axis element. The angular separation of the two beams is  $10.8^{\circ}$ . It is interesting to examine the theoretical values using simple Gaussian optics. The angular separation of the beams is



given by:  $\tan \phi = \frac{d\sqrt{2}}{f}$  and the 10 db beamwidth is given by  $2\tan^{-1}(1.072\frac{w_0}{f})$ , where  $w_0$  is the minimum waist of the beam coming out of the machined section,  $f$  is the focal distance of the lens inside the dewar and  $d$  is the minimum separation of the elements (for detectors #4 and #5 the separation is  $d\sqrt{2}$ ). For  $w_0 = 1.75 \text{ mm}$ ,  $f = 37 \text{ mm}$ ,  $d = 6.5 \text{ mm}$ , the expected angular separation is  $14^\circ$  and the 10 db beamwidth is  $5.8^\circ$ . Thus, the deviation from a pure Gaussian behavior is not significant. We can see for the off-axis element that a shoulder appears. This can be attributed to the aberrations introduced by the lens.

#### 4.4 Fourier Transform Spectroscopy (FTS) Measurements

The power coupling efficiency of the receiver was examined by FTS measurements. These take place while the detector is operating in video mode as we did for beam pattern measurements. Thus, the differential current is proportional to the power coupled to the receiver. We used a step-scan Michelson interferometer with an mercury lamp source and amplitude modulation technique. Although phase modulation is preferred in terms of SNR, amplitude modulation is easier to handle since there is always a background signal that can be detected. On the other hand, if the coupling is weak, it is hard to tell when constructive interference takes place because there is also the possibility that the mirrors used are somehow misaligned.

The principle of operation is simple. Let's assume that the spectrum of the source is large and uniform for our practical case. The Michelson interferometer is a two-beam interferometer, where constructive interference of a particular frequency takes place when the optical path difference of the two beams is an integer multiple of  $\lambda$ . For our broadband source, the power ( $P$ ) detected by the device of interest and the coupling efficiency ( $C$ ) are related by Fourier cosine transformation:

$$P(\delta) = \int_{-\infty}^{+\infty} C(\nu)\cos(2\pi\nu\delta)d\nu \Leftrightarrow C(\nu) = \int_{-\infty}^{+\infty} P(\delta)\cos(2\pi\nu\delta)d\delta \quad (4.5)$$

where  $\delta$  is the optical path difference or retardation and  $\nu$  is the wavenumber  $\frac{1}{\lambda}$ . In practice, the retardation is finite and the sampling is not continuous but discrete. The

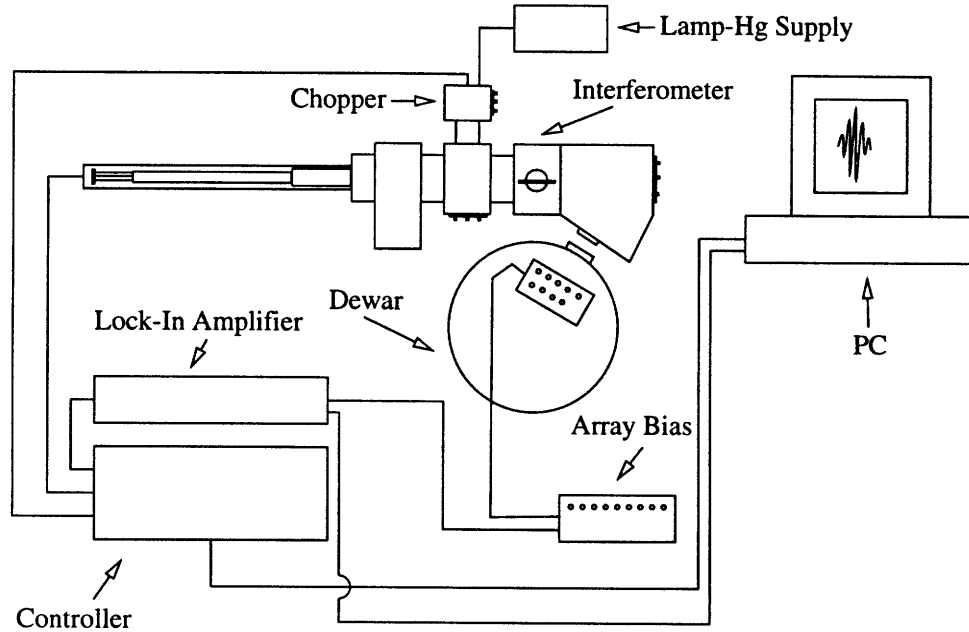


Figure 4-8: *Experimental set-up for FTS measurements.*

frequency resolution is inversely proportional to the maximum retardation and the bandwidth is inversely proportional to the sampling interval. FFT techniques have greatly facilitated the computation of  $C(\nu)$ . The bibliography about FTS measurements is rich, a simple textbook the reader is urged to look up is [43].

#### 4.4.1 Experimental Set-Up and Measurements

The cryogenic unit is placed near the interferometer with the two windows facing each other (Figure 4-8). The detector is biased in V-mode at I-V point just below the gap. The current level feeds the lock-in amplifier. A signal with the chopping frequency feeds also the lock-in amplifier. The locked differential current feeds the PC. The controller consists of the servomotor controller and the amplitude modulator controller. These regulate mainly the angular velocity of the piston which moves the mirror and the chopping frequency for amplitude modulation.

Different designs were tested. The  $140 \mu\text{m} - 190 \mu\text{m}$  design that we tested extensively in this project was measured and its coupling is illustrated in Figure 4-9. The 3 db beamwidth is 25 GHz and the maximum coupling occurs at 192 GHz. It is worth mentioning that the best noise performance was measured in the vicinity of this frequency. On the other hand,

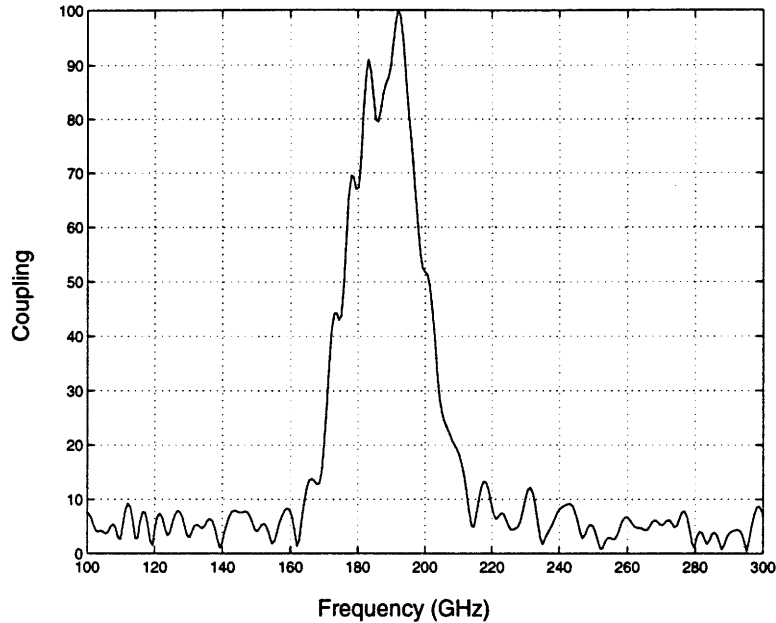


Figure 4-9: *FTS measurement of the 140  $\mu\text{m}$  - 190  $\mu\text{m}$  design.*

simulated results gave a bandwidth at least twice as much, assuming constant and resistive value of the antenna. Thus, we can deduce that the limiting factor is the antenna bandwidth.

## 4.5 Josephson Junction Local Oscillator (JJLO) Measurement

Some preliminary measurements of pumped and unpumped I-V characteristics have been made using the integrated JJLO. Instead of using the standard cryogenic unit, a dip-stick technique was applied and instead of an array, a single element was tested. A stick holding the examined chip is immersed in the He tank. The pads of the chip are connected to a modified chip holder with silver paint. Wires passing through the stick, connect the pads with external circuitry and measuring devices. A close-up of the stick in the area where the chip is located is illustrated in Figure 4-10. There are six pads; two of them are for the antenna, one for the control line which suppresses the Josephson effect, and the other three are used for biasing the JJLO and monitoring the output power via a RSJ (resistively shunted junction) detector.

The control line operated satisfactorily suppressing the Josephson effect. This new

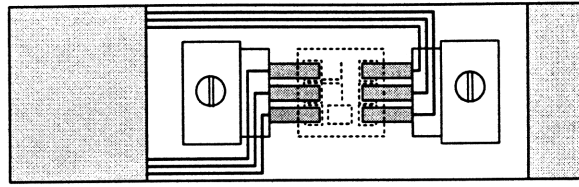


Figure 4-10: *Detail of the stick used for dip-stick measurements.*

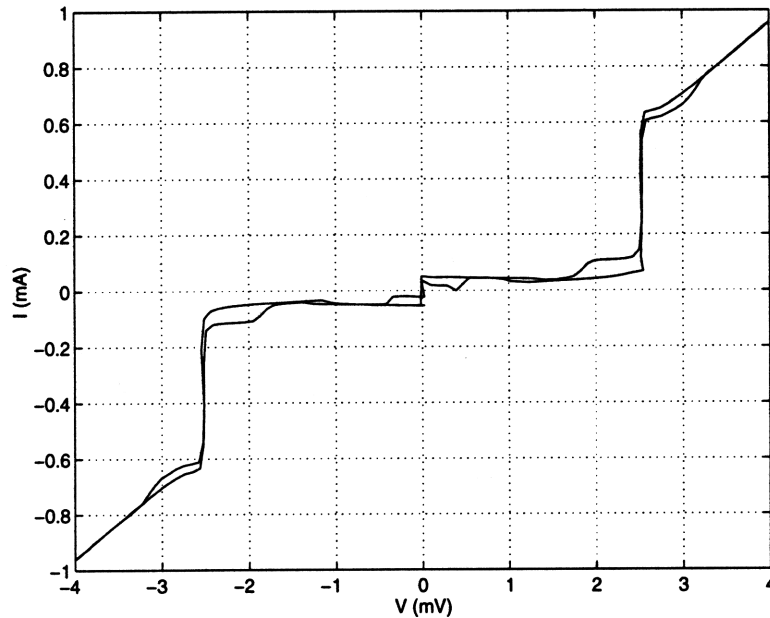


Figure 4-11: *Pumped and unpumped characteristic with integrated JJLO.*

feature is very useful for imaging purposes. The magnet we use for the array has the disadvantage that it affects all the detectors. Thus, a current setting can be optimum for a particular SIS but inadequate for another SIS. The individual control lines give the flexibility of independent optimization needed for imaging. The best measurement in terms of pronounced photon steps is given in Figure 4-11. We can make some rough estimates about the power level coupled to the device and the frequency of the JJLO signal. If we assume the quantum limit of responsivity  $\frac{\Delta I_{DC}}{\Delta P} = \frac{e}{\hbar\omega}$ , we can estimate the power level by measuring  $\Delta I_{DC}$  and the length of the first photon step  $\frac{\hbar\omega}{e}$ . We end up with a power level roughly 30 - 50 nW. The frequency, judging by the first photon step, is in the region of 190 GHz. As a comparison, for elements of the array that have been earlier presented, the LO power coupled for heterodyne measurements is roughly in the range 40 - 80 nW. Thus, we are very optimistic that a heterodyne measurement will yield good results.

# Chapter 5

## Conclusions - Future Work

### 5.1 Conclusions

A micromachined 3x3 array of SIS detectors has been designed, fabricated and tested.  $3\mu\text{m} \times 3\mu\text{m}$  SIS junctions with  $5\text{kA}/\text{cm}^2$  critical current density have been used. Bandwidth of 40 GHz has been measured and the best results have been reported in the vicinity of 190 GHz. The array has shown a uniformity of operation and the lowest noise temperature is measured to be within the range of 62 - 102 K, ranking our array among the best reported so far in this frequency region. Nevertheless, there is room for further improvements and advances in the design, fabrication, and measurement procedure.

### 5.2 Future Work

Multicolor detection will be the direct offspring of the current research. The design of the antenna must be properly scaled according to the frequency of interest. On the same device wafer will reside SIS mixers of different center frequencies of operation. Since the machined and micromachined sections are mostly responsible in determining the impedance seen by the antenna leads, they must be scaled too. Nevertheless, the scaling process must take into account that everything is done monolithically. Thus, a trade-off will be inevitable.

The linewidth of the JJLO signal must be measured using an external Gunn oscillator to produce a mixed signal at the IF frequency. Then, the IF signal can be directed to a

spectrum analyzer whereby the spectrum of the JJLO signal can be analysed. The linewidth of this signal is an important parameter for a successful mixer operation. Furthermore, the power level must not saturate the SIS detector or be too weak. Other coupling circuits can be tested for their effectiveness. They must be compact though, because of the limited space available on the device wafer.

An interesting and challenging issue will be the combination of multicolor detection and a satisfactory operation of the JJLO. In that way, the design of the JJLO must follow the frequency demand of the antenna of interest. The current system uses an external LO source that illuminates the entire array making multicolor operation impossible.

A limitation of the current set-up is the use of only one element for measuring the IF signal because of the the volume of the HEMT amplifier. Recent advances of small cryogenic preamplifiers which show high performance and low heat dissipation can facilitate the experimental process.

The environment of the experimental set-up was not ideal because external radiation can alter the measurements and multiple reflections from metallic objects can create undesirable standing waves. Ecosorb pieces were used but still the above problems can not be solved satisfactorily. Arifur Rahman and Erik Duerr have designed and implemented an anechoic chamber for millimeter wave measurements. With some minor modifications it will suit well the requirement for low-level external radiation.

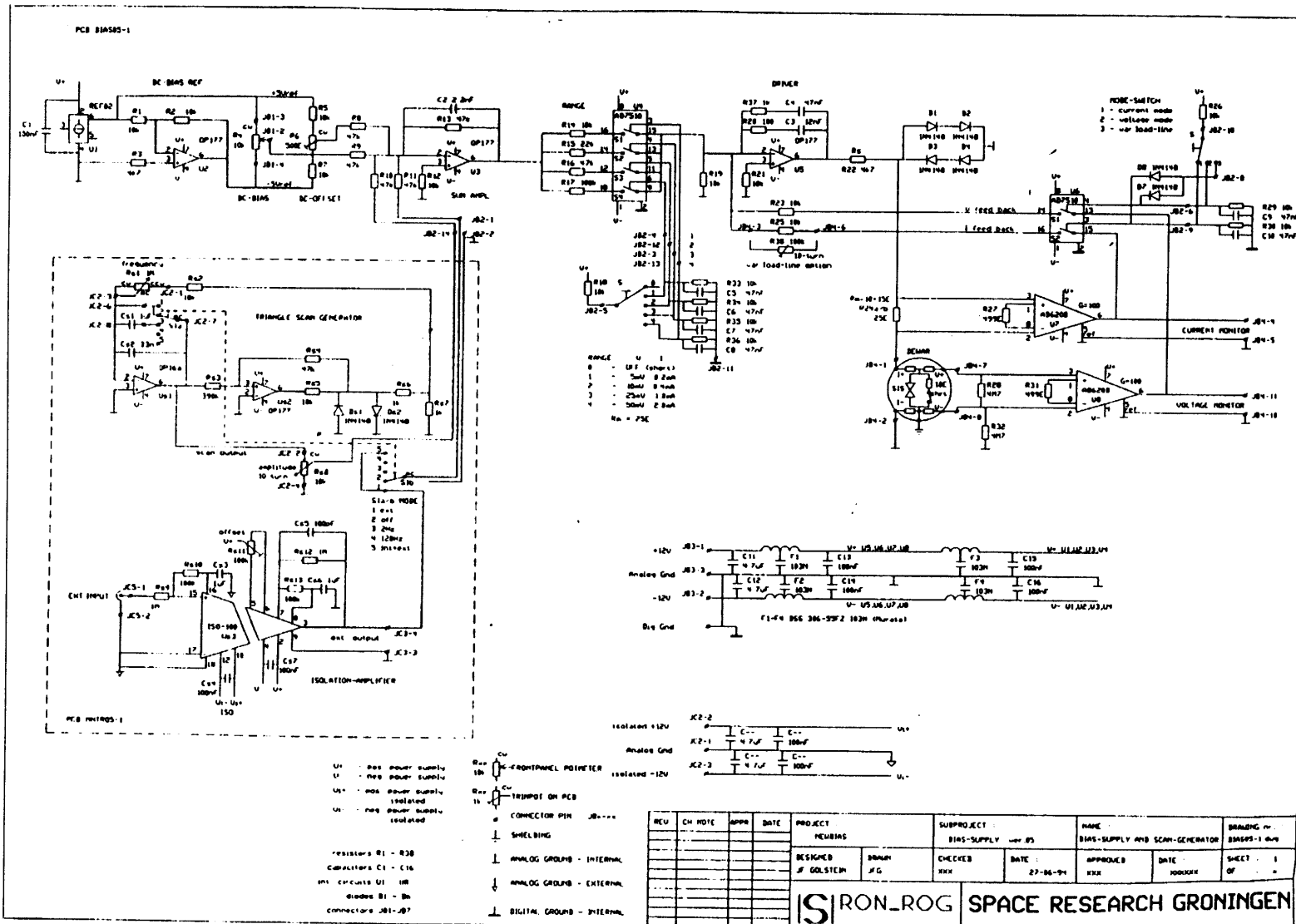
Since this research is oriented for focal plane array detectors, measurements for imaging purposes will be of great interest. Simple imaging measurements can be conducted using the video mode of the SIS detector. In that way, figures with high contrast of hot (300 K) and cold (77 K) loads can be used in this first stage to prove the imaging properties of the array. For the case of wide angle detection, the cryogenic unit must be rotated in a controlled way. Thus, a computer-controlled rotational stage is important.

The optics used had the characteristic of simplicity. The major drawback is that the beams don't leave the dewar window in a parallel fashion. Other approaches can be adopted for better performance (individual semispherical lenses, mirrors inside the dewar etc). Time must be spent for analysing the pros and cons of different ideas since the complexity must be kept as low as possible inside the cryogenic unit where space is limited.

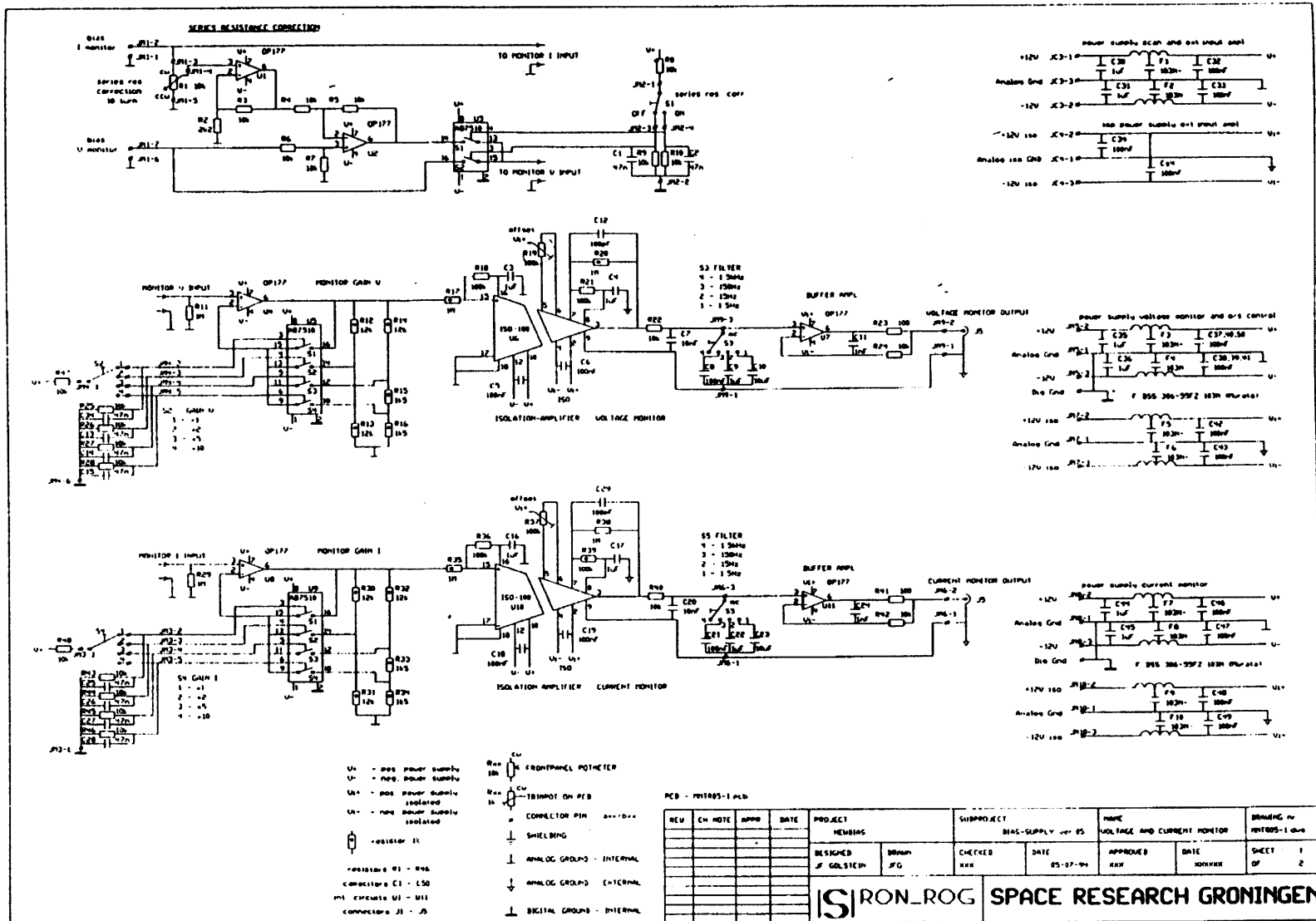
# **Appendix A**

## **Biassing Circuitry**

The complete circuit diagram of the biassing box, courtesy of SRON, is presented here (module 1 and module 2).









# Bibliography

- [1] Al Pergande, Don Dean, and Dan O'Donnel. Passive millimeter wave imaging. In *Proceedings of SPIE*, volume 2736 of *SPIE Enhanced and Synthetic Vision*, page 240. International Society of Optical Engineers (SPIE), 1996.
- [2] Paul W. Kruse. Why the military interest in near-millimeter wave imaging? In *Proceedings of SPIE*, volume 259 of *Millimeter Optics*, page 94. Proc. Soc. Photo-Opt. Instrum. Eng., 1980.
- [3] D. M. Sheen, H. D. Collins, R. P. Gribble, and D. L. McMakin. Comparison of active millimeter-wave and acoustic imaging for weapon detection. In *Proceedings of SPIE*, volume 2935 of *SPIE Surveillance and Assessment Technologies for Law Enforcement*, page 120. International Society of Optical Engineers (SPIE), 1996.
- [4] John O. Hooper. Passive millimeter wave imaging for guidance applications. In *Proceedings of SPIE*, volume 423 of *SPIE Millimeter Wave Technology II*, page 74. International Society of Optical Engineers (SPIE), 1983.
- [5] Holger H. Meinel. Commercial applications of millimeterwaves. History, present, status and future trends. *IEEE Trans of Microwave Theory and Techn.*, 43:1639, 1995.
- [6] Holger H. Meinel. Recent advances on millimeterwave PCN system development in Europe. An invited survey. In *Proceedings of 1995 IEEE MTT-S International Microwave Symposium*, volume 2, page 401. IEEE MTT-S International Microwave Symposium Digest, 1995.
- [7] Gerhard de Lange. *Quantum Limited Heterodyne Detection of 400-800 GHz Radiation with Superconducting Nb Tunnel Junctions*. PhD dissertation, The University of Groningen, Department of Applied Physics, 1994.
- [8] H. Suzuki, T. Imamura, N. Yokoyama, M. Suzuki, H. Ogawa, K. Kawabata, and Y. Fukui. Applications of mm-wave SIS mixers to middle atmosphere monitoring systems. *IEEE Trans. on Applied Superconductivity*, 5:3296, 1995.
- [9] Jr. N. C. Luhmann. Instrumentation and techniques for plasma diagnostics: an overview. In Kenneth J. Button, editor, *Infrared and Millimeter Waves*, volume 2, chapter 1, page 1. Academic Press, 1979.

- [10] D. Véron. Submillimeter interferometry of high density plasmas. In Kenneth J. Button, editor, *Infrared and Millimeter Waves*, volume 2, chapter 2, page 67. Academic Press, 1979.
- [11] J. R. Tucker. Predicted detection in nonlinear tunneling devices. *Applied Physics Letters*, 33:611, 1978.
- [12] J. R. Tucker. Predicted conversion gain in superconductor-insulator-superconductor quasiparticle mixers. *Applied Physics Letters*, 36:477, 1980.
- [13] G. de Lange, B. R. Jacobson, and Q. Hu. A low-noise micromachined millimeter wave heterodyne mixer with Nb superconducting tunnel junctions. *Applied Physics Letters*, 68:1862, 1996.
- [14] E. Garcia, B. R. Jacobson, and Q. Hu. Fabrication of high quality superconductor-insulator-superconductor junctions on thin  $Si_3N_4$  membranes. *Applied Physics Letters*, 63:1002, 1993.
- [15] G. de Lange, A. Rahman, E. Duerr, and Q. Hu. Development of a 3x3 micromachined millimeter wave SIS imaging system. *IEEE Trans. on Applied Superconductivity*, 7:3593, 1997.
- [16] David B. Rutledge and Michael S. Muha. Imaging antenna arrays. *IEEE Trans. on Antennas and Propagation*, 30:535, 1982.
- [17] G. V. Eleftheriades. *Analysis and Design of Integrated-Circuit Horn Antennas for Millimeter and Submillimeter-Wave Applications*. PhD dissertation, The University of Michigan, Department of Electrical Engineering, 1993.
- [18] James P. Hollinger. Applications of millimeter wave imaging. In *Proceedings of SPIE*, volume 544 of *SPIE Millimeter Wave Technology III*, page 118. International Society of Optical Engineers (SPIE), 1985.
- [19] A. V. Raisanen, W. R. McGrath, P. L. Richards, and F. L. Lloyd. Broad-band RF match to a millimeter-wave SIS quasi-particle mixer. *IEEE Trans of Microwave Theory and Techn.*, 33:1495, 1985.
- [20] T. H. Buttgenbach, H. C. LeDuc, P. D. Maker, and T. G. Phillips. A fixed tuned broadband matching structure for submillimeter astronomy. *IEEE Trans. Appl. Superconductivity*, 2:165, 1992.
- [21] V. P. Koshelets, A. V. Shchukin, S. V. Shitov, and L. V. Fillipenko. Superconducting millimeter wave oscillators and SIS mixers integrated on a chip. *Applied Superconductivity Conference*, 1992.
- [22] A. R. Kerr, S. K. Pan, and A. W. Lichtenberger. Progress on tunerless SIS mixers for the 200-300 GHz band. *IEEE Microwave and Guided Wave Letters*, 2:454, 1992.

- [23] Jacob W. Kooi, M. Chan, T. G. Phillips, and H. G. LeDuc. A low noise 230 GHz heterodyne receiver employing  $.25\mu m^2$  area  $Nb/AlO_x/Nb$  tunnel junctions. *IEEE Trans of Microwave Theory and Techn.*, 40:812, 1992.
- [24] J. W. Kooi, M. Chan and B. Bumble, H. G. LeDuc, P. L. Schaffer, and T. G. Phillips. 180-425 GHz low noise SIS waveguide receivers employing tuned  $Nb/AlO_x/Nb$  tunnel junctions. *International Journal of Infrared and Millimeter Waves*, 5:783, 1994.
- [25] J. Bardeen, L. N. Cooper, and J.R Schrieffer. Theory of superconductivity. *Physical Review*, 108:1175, 1957.
- [26] John R. Tucker and Mark J. Felman. Quantum detection at millimeter wavelengths. *Reviews of Modern Physics*, 57:1055, 1985.
- [27] Arifur Rahman. Room temperature micromachined microbolometers for W-Band (75 GHz-110 GHz) focal plane imaging array. MS thesis, Massachusetts Institute of Technology, Department of Electrical Engineering and Computer Science, 1996.
- [28] George V. Eleftheriades and Gabriel M. Rebeiz. Design and analysis of quasi-integrated horn antennas for millimeter and submillimeter-wave applications. *IEEE Trans of Microwave Theory and Techn.*, 41:954, 1993.
- [29] W. Y. Ali Ahmad, G. V. Eleftheriades, L. P. Katehi, and G. M. Rebeiz. Millimeter-wave integrated-horn antennas. Part II: Experiment. *IEEE Trans. on Antennas and Propagation*, 39:1582, 1991.
- [30] George V. Eleftheriades and Gabriel M. Rebeiz. High-gain step-profiled integrated diagonal horn-antennas. *IEEE Trans of Microwave Theory and Techn.*, 40:801, 1992.
- [31] G. V. Eleftheriades, W. Y. Ali Ahmad, L. P. Katehi, and G. M. Rebeiz. Millimeter-wave integrated-horn antennas. Part I: Theory. *IEEE Trans. on Antennas and Propagation*, 39:1575, 1991.
- [32] Gert de Lange, Qing Hu, Howard Huang, and Arthur W. Lichtenberger. Development of a 170-210 GHz 3x3 micromachined SIS imaging array. In *Proceedings of the Eighth International Symposium on Space Terahertz Technology*, page 518, 1997.
- [33] T. Van Duzer and C. W. Turner. *Principles of Superconductive Devices and Circuits*. Elsevier, 1981.
- [34] Anthony E. Siegman. *Lasers*. University Science Books, 1986.
- [35] Paul F. Goldsmith. Quasi-optical techniques at millimeter and submillimeter wavelengths. *Infrared and Millimeter Waves*, 6:277, 1982.
- [36] HYPRES Inc, 175 Clearbrook Road, Elmsford, NY 10523. *Niobium Design Rules*.

- [37] Arthur W. Lichtenberger, Dallas M. Lea, Robert J. Mattauch, and Frances L. Lloyd. *Nb/Al-Al<sub>2</sub>O<sub>3</sub>/Nb* junctions with inductive tuning elements for a very low noise 205-250 GHz heterodyne receiver. *IEEE Trans of Microwave Theory and Techn.*, 40:816, 1992.
- [38] Brian Ratcliff Jacobson. A micromachined SIS mixer. MS thesis, Massachusetts Institute of Technology, Department of Electrical Engineering and Computer Science, 1994.
- [39] D. W. Denlinger, E. N. Abarra, Kimberly Allen, P. W. Rooney, M. T. Messer, S. K. Watson, and F. Hellman. Thin film microcalorimeter for heat capacity measurements from 1.5 to 800 K. *Rev. Sci. Instrum.*, 65:946, 1994.
- [40] James W. Lamb. Infrared filters for cryogenic receivers. Technical report, National Radio Astronomy Observatory, 1992.
- [41] Infrared Laboratories Inc, 1808 East 17th Street, Tucson, AZ 85719. *Model HD-3 Helium Dewar*.
- [42] Gert de Lange, Konstantinos Konistis, Qing Hu, Ray Robertazzi, and David Osterman. A low-noise, 9-element micromachined SIS imaging array. In *Proceedings of the Ninth International Symposium on Space Terahertz Technology*, 1998.
- [43] Peter R. Griffiths and James A. de Haseth. *Fourier Transform Infrared Spectrometry*. Wiley Interscience Publication, 1986.